Ocean Modelling 25 (2008) 154–171

Contents lists available at ScienceDirect

Ocean Modelling

journal homepage: www.elsevier.com/locate/ocemod

# A global wave parameter database for geophysical applications. Part 1: Wave-current–turbulence interaction parameters for the open ocean based on traditional parameterizations

Nicolas Rascle [a,b], Fabrice Ardhuin [a,*], Pierre Queffeulou [c], Denis Croizé-Fillon [c]

[a] Centre Militaire d'Océanographie, Service Hydrographique et Océanographique de la Marine, 29609 Brest, France
[b] Laboratoire de Physique des Océans, Université de Bretagne Occidentale, 29000 Brest, France
[c] Laboratoire d'Océanographie Spatiale, Ifremer, 29280 Plouzané, France

ARTICLE INFO

*Article history:*
Received 28 December 2007
Received in revised form 3 July 2008
Accepted 18 July 2008
Available online 12 August 2008

*Keywords:*
Surface gravity waves
Air–sea fluxes
Surface drift
Ocean mixing

ABSTRACT

Ocean surface mixing and drift are influenced by the mixed layer depth, buoyancy fluxes and currents below the mixed layer. Drift and mixing are also functions of the surface Stokes drift $U_{ss}$, volume Stokes transport $T_S$, a wave breaking height scale $H_{swg}$, and the flux of energy from waves to ocean turbulence $\Phi_{oc}$. Here we describe a global database of these parameters, estimated from a well-validated numerical wave model, that uses traditional forms of the wave generation and dissipation parameterizations, and covers the years 2003–2007. Compared to previous studies, the present work has the advantage of being consistent with the known physical processes that regulate the wave field and the air–sea fluxes, and also consistent with a very large number of *in situ* and satellite observations of wave parameters. Consequently, some of our estimates differ significantly from previous estimates. In particular, we find that the mean global integral of $\Phi_{oc}$ is 68 TW, and the yearly mean value of $T_S$ is typically 10–30% of the Ekman transport, except in well-defined regions where it can reach 60%. We also have refined our previous estimates of $U_{ss}$ by using a better treatment of the high frequency part of the wave spectrum. In the open ocean, $U_{ss} \simeq 0.013U_{10}$, where $U_{10}$ is the wind speed at 10 m height.



## 1. Introduction

Waves constitute the essential gearbox between the atmosphere and ocean, allowing large fluxes of energy, momentum, and gases across the air–sea interface. The variability of common wave properties such as the significant wave height $H_s$ or the mean period $T_{m02}$ is well known and widely used for navigation safety or ocean engineering. However, for other purposes, such as atmosphere or ocean modelling, several key parameters are poorly known. For example, the magnitude of the fluxes of energy from the atmosphere to the wave field is poorly known. In a review of the global ocean energy budget, Wunsch and Ferrari (2003) give a value of 20 TW for the global average of the wind to wave energy flux, which was revised by Wang and Huang (2004) to 60 TW. As will be shown here this is still probably underestimated. Given the recent interest in storm-induced mixing Quéré et al., 2007;Sriver and Huber, 2007;Liu et al., 2008, a precise estimation of the wave-related components and fluxes in the Earth system is needed.

The ocean surface layer is influenced by different characteristics of the waves. These waves cover a vast range of scales, from individual waves over 30 m high and wavelengths over 400 m, to short capillary-gravity waves of a few centimeters in height and wavelength. Such a complex multi-scale forcing may be characterized using a few key parameters. These include the surface Stokes drift $U_{ss}$, and a scale $H_{swg}$ for the height of large breaking waves which likely controls the sub-surface level of turbulence together with the rate of waves energy dissipation per unit surface $\Phi_{oc}$. A few estimates of these parameters have been published, usually based on indirect measurements with a limited set of observations (e.g., Stacey and Pond, 1997). In order to extrapolate these estimates to general conditions, assumptions are often called upon without a clear understanding of their consequences. In particular, the wave age that characterizes the development of the sea state, is of critical importance for a precise estimation of the Stokes drift and the breaking wave height. Nevertheless, the wave field is often assumed to be a fully developed windsea (e.g., McWilliams and Restrepo, 1999), although this may well be the least likely type of sea state. Indeed, in several years of data, Pierson and Moskowitz (1964) could only find about 20 instances of fully developed seas (Alves et al., 2003).

* Corresponding author.
*E-mail address:* ardhuin@shom.fr (F. Ardhuin).

1463-5003/$ - see front matter © 2008 Elsevier Ltd. All rights reserved.
doi:10.1016/j.ocemod.2008.07.006

In the absence of any other information, the ocean circulation modeler is left to extrapolate these parameter values in uncharted waters, with likely large errors. An interesting parallel is provided by the problem of the estimation of the wind stress over the ocean, a parameter measured much more frequently than surface drift or near-surface turbulence. Drennan et al. (2005) clearly showed that empirical relations derived for deep water conditions were unable to reproduce the Risø air–sea exchange (RASEX) shallow water wind stresses, because these simple analytical expressions do not include mechanical constraints on the wind stress, i.e., energy and momentum must be passed to the ocean through the waves in a way consistent with their known physical properties. A numerical wave model, even if based on an imperfect knowledge of the detailed physical processes, will capture at least some of these constraints. A model may thus provide the best estimate of the wave spectrum and the energy fluxes in and out of the wave field, in a way consistent with wave observations.

In return, waves are significantly influenced by oceanic currents with velocities larger than a sizeable fraction of the wind or wave phase speed (i.e., larger than about 30 cm $s^{-1}$). Some of these effects are discussed in the present paper. However, because high quality surface current information at global scale is not yet available (see e.g., Collard et al., 2008, for a discussion of errors in surface current observations and models), the results discussed here do not include the effects of surface currents. This correction is left for future work.

A preliminary estimation of the atmosphere–wave–ocean fluxes at global scales, including $\Phi_{oc}$, and of the Stokes volume transport $T_S$, was performed by Janssen et al. (2004). However, values were only given for the month of January 2003. Further, that model only resolved explicitly waves of periods larger than 2.5 s, i.e., waves longer than 10 m. As a result, windseas for winds with a 10 m velocity $U_{10}$ under 5 m $s^{-1}$ are very poorly modelled. Following recent improvements in numerical wave models at the global scale (e.g., Janssen, 2008), we extend that study and provide a general global and regional-scale database of wave-related parameters. Although better parameterizations have been proposed very recently (e.g., Ardhuin et al., 2008a,b), we prefer to make this first version of our database using the more traditional parameterizations given by Bidlot et al. (2007a). For applications to coastal or enclosed seas, the method used here would typically need to be applied using a higher resolution model, as we have done for the Bay of Biscay (these higher resolution results are not used in the data presented here).

In Section 2, we review the parameters needed to represent the wave-induced mixing and surface drift. The numerical wave model and its validation in terms of commonly observed quantities such as the significant wave height $H_s$ and mean period $T_{m02}$ are described in Section 3, with a brief discussion of problems and sources of errors. In Section 4, we then discuss in turn each of these parameters and provide a fresh estimation of their magnitude and variability. All wave-related parameters are highly variable in time and space due to the intermittent nature of the wave field. In this context, averages may not be meaningful, even in terms of order of magnitude. We thus encourage the reader to access our database at ftp://ftp.ifremer.fr/ifremer/cersat/products/gridded/wavewatch3/, instead of stopping at the crude relationships, reviewed here, that relate these parameters to the local wind speed. A short guide to the database is given in Appendix A. Better still, running a wave model is simple enough and should be done when investigating the ocean circulation at regional scales. The necessary input files and model setup are also provided in the database with the end results over a few regions. We then present, in Section 5, some illustration of the usage of this data for the modelling of the ocean mixed layer, and finish with a brief introduction to the ongoing improvements and extensions of the database.

## 2. Which parameters for wave-induced mixing?

The classical view on the ocean surface layer is a transposition of the atmospheric boundary layer over land, which is well described by Monin-Obukhov theory, as verified in the Kansas experiments (Businger et al., 1971). Turbulent kinetic energy (TKE) is produced by velocity shears and unstable stratification, and may be destroyed by stable stratification and viscous dissipation. In stably stratified cases, the mixed layer depth (MLD) results from a balance between the shear production by the mean current and the buoyancy damping, represented by their ratio, the Richardson number.

A significant difference in the ocean surface layer is that the surface is neither rigid nor flat due to the presence of waves. Since the early 1990s many field experiments have demonstrated that waves profoundly modify the ocean surface layer (e.g., Agrawal et al., 1992), with no counterpart in the atmospheric boundary layer. Although the momentum flux profiles generally agree with the land data in the mean (Fairall et al., 2003), deviations are also evident at low and high wind, showing a clear departure from Monin-Obukhov theory, due to a variety of wave-related processes (e.g., Sullivan et al., 2008).

First, the surface generation of TKE associated with wave breaking dominates by far the near-surface TKE production by the current shear (e.g., Terray et al., 1996). This strongly modifies the classical balance of shear production and buoyancy damping. For instance, Noh (1996) showed that this surface flux of turbulence is a necessary ingredient to obtain a thermocline in the presence of both wind and stabilizing buoyancy flux. This explains why the diurnal ocean surface layer exhibits a thermocline, while the nocturnal atmospheric boundary layer, its atmospheric counterpart, does not.

Second, most of the momentum flux $\tau_a$ from the atmosphere to the ocean transits through the wave field, with an input given by the form drag (or wave-supported stress) $\tau_w$ and an output to the current field in the form of wave breaking $\tau_{oc}$. Only a small fraction of $\tau_a$, except at very low winds, goes directly from the atmosphere to the ocean via the mean viscous stress at the surface (Dobson, 1971; Snyder et al., 1981; Donelan, 1998). However, most of the momentum flux is rapidly passed to the currents as waves break.

Technically, the wind stress applied to the ocean for computing the mean current should be reduced to $\tau_{oc}$, to account for the fraction radiated away by the wave field, but this is typically less than 3% of $\tau_a$ (Donelan, 1998; Janssen et al., 2004). Nevertheless, even if most of the momentum and energy gained by the waves is quickly released to the ocean (Donelan, 1998), the small fraction radiated in the wave field is important. First of all, it is the energy that is eventually dissipated in the surf, and available for potential conversion to electric power. Further, from an ocean circulation point of view, the associated wave momentum[1] radiated with the wave field further interacts with the mean flow.

### 2.1. Wave-induced mixing in the near-surface zone

Whitecaps at the ocean surface provide an intense source of TKE compared to the shear of the mean current (Terray et al., 1996). This process has been successfully modelled with simple two-equation models for the turbulence closure (e.g., Mellor and Yamada, 1982), by adding the TKE surface flux $\Phi_{oc}$ coming from the dissipation of surface waves and by setting the near-surface mixing length at the surface $z_0$ to a relatively large value, of the order of the

[1] The phrase wave momentum is used here instead of the correct wave pseudo-momentum, the reader is referred to McIntyre (1981) for a detailed discussion of these concepts.

significant wave height $H_s$ (Craig and Banner, 1994; Terray et al., 1996; Burchard, 2001; Acreman and Jeffery, 2007). This wave height should be further restricted to the windsea only since swells do not break in deep water, and may also be a function of the wave age (see Section 4.3). Given the ongoing debate on the scaling of $z_0$ we did not go further the straightforward estimation of the windsea wave height $H_{swg}$, defined below, leaving to ocean modelers the choice of the exact parameterization of $z_0$ from this height scale.

In summary, the modelling of ocean near-surface mixing requires the flux of TKE to the oceanic turbulence $\Phi_{oc}$, and the sub-surface roughness $z_0$, with a proxy given by $H_{swg}$.

### 2.2. Wave-induced mixing through the whole mixed layer

The wave momentum and its interactions with the current are also known to be at the origin of Langmuir circulations (Langmuir, 1938; Craik and Leibovich, 1977; Garrett, 1976), which are believed to constitute the dominant vertical mixing mechanism for momentum and tracers over the entire mixed layer (Smith, 2001; Noh et al., 2004), and an important process for deepening the mixed layer (Li et al., 1995).

Langmuir turbulence is reported to occur for small values of the Langmuir parameter $La = \sqrt{u_{\star}/U_{ss}}$, where $u_{\star}$ is the air-side friction velocity, and observations suggest that the turbulent velocity $w_{rms}$ scales with the surface Stokes drift (Smith, 1998). We note that the vertical shear of the Stokes drift is absent from these dimensional analysis, whereas the tilting of the vorticity of the current by the Stokes drift shear is a key ingredient in recipes for Langmuir circulation. Recently, Harcourt and D'Asaro (2008) proposed a revised Langmuir parameter $La_{St}$, in which the mean Stokes drift between the surface and one fifth of the MLD is used instead of its surface value. That number was chosen to include in the dimensional analysis the ratio of the MLD to the Stokes depth, which characterizes the vertical shear of the Stokes drift through the mixed layer. Based on large eddy simulations (LES), the turbulent velocity of the Langmuir cells was found to depend on that modified Langmuir number by the formula $w_{rms} \propto u_{\star} La_{St}^{-2/3}$. These authors further argued that the observations hardly exhibit such a trend because of inverse correlations between winds speeds and wave ages in the field measurements.

Thus a proper parameterization of the sub-surface mixing requires estimations of the vertical profile of the Stokes drift vector. At the very least, this may be reduced to its surface value $U_{ss}$, with a measure of the shear given by the combination of $U_{ss}$ and the wave-induced volume transport $T_S$. Besides, the TKE produced by the straining of turbulence due to the wave field, of the order of $\tau_a U_{ss}$ (Ardhuin and Jenkins, 2006) gives an upper bound on the flux of energy from the waves to the Langmuir circulation, an amount of energy partly available for the erosion of the thermocline. The fraction of that energy flux actually used to increase the MLD may be better defined by analyzing the contribution of the different scales of Langmuir rolls to the vertical flux of momentum. One would expect that, with a fraction $p$ of momentum flux carried by the biggest rolls, the TKE flux penetrating to the base of the mixed layer is of the order of $p\tau_a U_{ss}$.

### 2.3. Wave-induced drift and transport

Although the time-average transport due to waves is cancelled by the Stokes-Coriolis force (Hasselmann, 1970; Xu and Bowen, 1994; Ardhuin et al., 2004; Rascle et al., 2006), a proper modelling of surface drift does require an estimate of the surface Stokes drift $U_{ss}$. The Stokes volume transport $T_S$ may be used to diagnose an upper bound on the possible non-stationary wave-induced transport. The wave-induced mass transport $M^w = \rho_w T_S$, where $\rho_w$ is the water density, also comes into the general wave-current interaction equations, whether formulated in terms of the total momentum (Phillips, 1977) or in terms of the mean flow momentum only (Garrett, 1976; Smith, 2006; Ardhuin et al., 2008c).

## 3. Wave model and validation of standard parameters

### 3.1. Model description

All these parameters, $\Phi_{oc}$, $H_{swg}$, $U_{ss}$, and $T_S$ may be obtained from numerical wave models. One should be careful that such models are mostly verified in terms of significant wave height $H_s$ and peak or mean period only ($T_p$ or $T_{m02}$), so that other parameters, in particular those related to the high-frequency end of the spectrum may not be well estimated and noisy. This aspect should be considerably improved in the future versions of the database as the model parameterizations are refined. The results shown here are obtained with the WAVEWATCH III (WWATCH) code in its version 3.13 (Tolman, 2007), using the parameterization of Bidlot et al. (2005), later reviewed by Bidlot et al. (2007a) and Janssen (2008), for deep water processes, with the addition of a Battjes and Janssen (1978) parameterization for wave breaking in shallow water. In practice, this is activated with the `ST3` switch, and we further set the wind-wave growth parameter $\beta_{max}$ to 1.25 via the `SIN3` namelist. All other model parameters are default values. The code was further modified to allow the calculation and output of $\Phi_{oc}$, $H_{swg}$, $U_{ss}$, and $T_S$. This modification will likely be included in a later version of WWATCH, and is otherwise available from the authors.

Our model configuration is global (80°S to 80°N) with 1° resolution, using a combination of ETOPO5 data for the bathymetry (Sloss, 1993), and the GSHHS coastline database (Wessel and Smith, 1996) for producing the blocking mask which is used to represent subgrid islands (Tolman, 2003). The modelled spectra are discretized with 24 directions, and 32 frequencies $f$ exponentially spaced between 0.037 Hz and $f_{max}$ = 0.72 Hz. However, for $f > f_c$, a diagnostic tail proportional to $f^{-5}$ is imposed. We define $f_c$ as the maximum of 2.5 times the mean wind sea frequency (see Bidlot et al., 2005) and 4 times the peak frequency defined from the local wind.

This model is forced with 6h analysis of $U_{10}$ and daily sea ice concentrations from the European Center for Medium-Range Weather Forecasting (ECMWF). This particular model and configuration have been extensively validated against all *in situ* sensors reporting to the World Meteorological Organization (WMO) Global Transmission System, and all satellite altimeters (see Appendix B for methods) over the period January 2004 to December 2007, which is covered by the database. Further validation with SAR wave mode (Kerbaol et al., 1998) and image mode data (Collard et al., 2005) will be presented elsewhere. This model configuration (code, bathymetry and forcing) was chosen because, without using wave data assimilation, it gave the lowest root mean square errors (RMSE) on significant wave heights at buoys as illustrated in Fig. 1, and the smallest random errors against altimeter measurements (Fig. 2). This configuration is also close to that derived from version 2.22 of WWATCH, with results reported in Bidlot et al. (2007b).

*In situ* and altimeter data provide complementary views of the quality of the wave field. Buoys have a very good time resolution and provide information on both the energy content of the wave field, represented by $H_s$, and the wave scales represented by the mean or peak period, or the full frequency spectrum when available. Many buoys also measure wave directional properties. Unfortunately, buoys are generally deployed in coastal waters, in areas poorly resolved in a global model. Although the sea state in coastal areas is largely dominated by global scale wave fields, a proper validation would require an additional post-processing of the global model presented here, using nested coastal models, for example

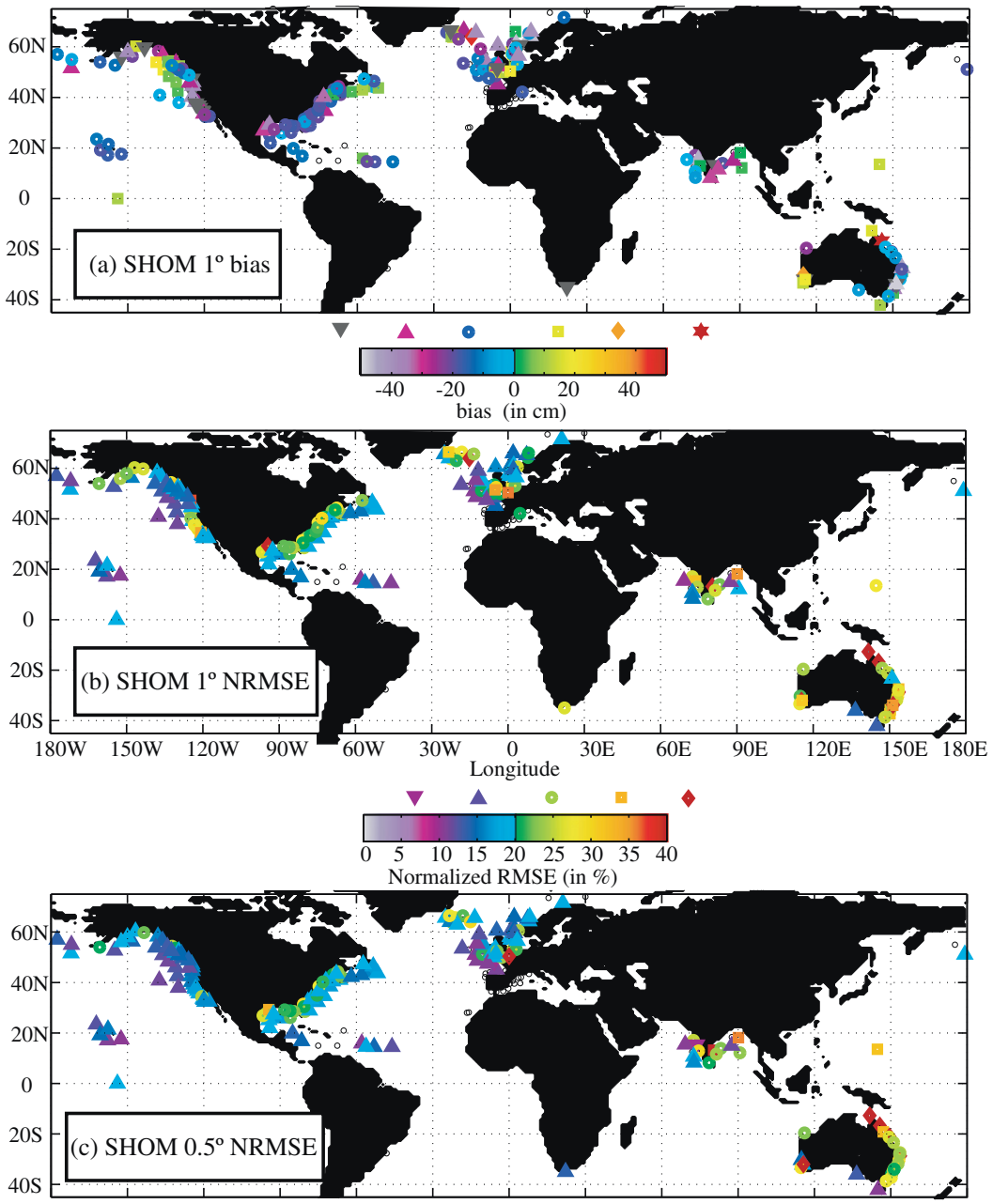


**Fig. 1.** Statistics for the year 2006. (a) Bias for $H_s$ at 214 *in situ* locations. Symbols ▽, △, ○, □, ◇ and ☆ correspond to values in the ranges $x < -50$, $-50 \leqslant x < -25$, $-25 \leqslant x < 0$, $0 \leqslant x < 25$, $25 \leqslant x < 50$, $50 \leqslant x$, respectively. (b) Normalized RMSE for $H_s$ at *in situ* locations. Symbols ▽, △, ○, □, and ◇ correspond to values in the ranges $0 \leqslant x < 10$, $10 \leqslant x < 20$, $20 \leqslant x < 30$, $30 \leqslant x < 40$, $40 \leqslant x$. (c) Same as (b) but for a higher resolution model.

based on ray-tracing, and potentially including specific coastal processes (e.g., Ardhuin et al., 2003; Magne et al., 2007). Further, many regions of the world are poorly instrumented, and, when they are, the data is often not reported to the WMO or other exchange programs sponsored by the International Oceanographic Commission (IOC). We have thus chosen to use the WMO-IOC Joint Commission on Oceanography and Marine Meteorology (JCOMM) intercomparison data for the year 2006 (Bidlot et al., 2002, 2007b) which includes 214 buoys and platforms, with data for $H_s$ and $T_p$ or $T_{m02}$ (depending on instrumentation packages), averaged over a 5 h window every 6 h (Bidlot and Holt, 2006). More detail on these instruments (location, instrumentation), and further model validation ca be found at http://www.jcomm-services.org/Wave-Forecast-Verification-Project.html. The model version used here corresponds to the SHOM model used between November and December 2007, for which results are shown on the JCOMM web site.

The 1° model configuration used here gives a generally negative bias of the order of 10 cm (Fig. 1a), and a normalized root mean square errors (NRMSE[2]) between 10% and 25% at most locations (Fig. 1b and c, Table 1).

Errors are largest at coastal buoys, some of which are in shallow water down to 20 m, mostly due to the coarse discretization of the coastline in the model. Using a 0.5° model show a general reduction of the errors (Fig. 1c), with a NRMSE that is, on average, 2.6% point above the ECMWF operational analysis (in which altimeter data is assimilated). Our use of a coastline to define subgrid islands, instead of a bathymetry data, is the likely reason for a better performance of the present model at several Australian buoys and the island of Guam, compared to ECMWF operational analysis

[2] This is the RMS difference divided by the RMS observation of a given location.

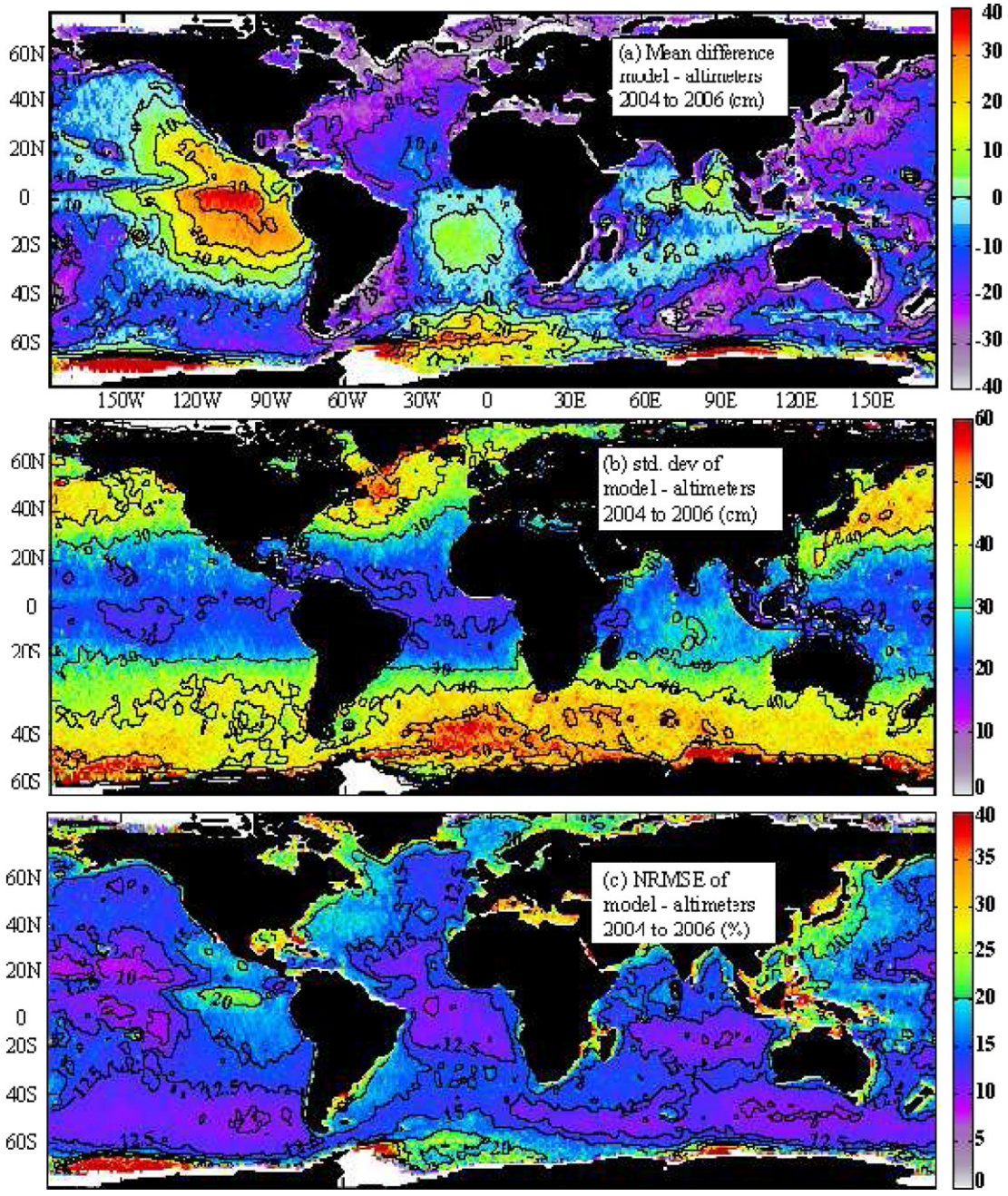


**Fig. 2.** Statistics for 2004–2006, combining data from JASON, ENVISAT and GEOSAT-Follow On (GFO). See Appendix B for satellite data analysis methods.

**Table 1**
Percentage of buoys with a given statistical parameter $x$ in a given range of values

| Model | Parameter | $x < 10$ | $\leqslant x < 20$ | $\leqslant x < 30$ | $\leqslant x < 40$ | $\leqslant x$ |
|---|---|---|---|---|---|---|
| SHOM 1° | NRMSE for $H_s$ | 0 | 51 | 36 | 8 | 5 |
| SHOM 1° | NRMSE for $T$ | 9 | 41 | 34 | 11 | 4 |
| SHOM 0.5° | NRMSE for $H_s$ | 1 | 63 | 29 | 3 | 3 |
| SHOM 0.5° | NRMSE for $T$ | 9 | 39 | 36 | 13 | 4 |
| ECMWF | NRMSE for $H_s$ | 12 | 62 | 17 | 3 | 6 |
| ECMWF | NRMSE for $T$ | 11 | 60 | 10 | 4 | 6 |

For reference, results from the operational ECMWF analysis are also given.

(not shown). However, for our present purpose, a global-scale climatology of wave-related parameters, it is most important to verify the quality of the model in the open ocean. Using data from three altimeter missions over the period 2004–2006 provides a large validation data base with enough data in 1° by 1° squares (the model resolution) to allow the estimation of reliable statistics (Fig. 2, see Appendix B).

In the open ocean the biases and random errors are typically larger on the western part of ocean basins. The altimeter also reveals particularly well a large bias in wave heights in the Eastern Pacific. This bias is clearly associated with the WAM-type dissipation and input parameterizations (Komen et al., 1984), since it was already present in WAM Cycle 3 (Tolman, 2002, Fig. 5), and was only slightly reduced with the latest ECWAM parameterization (Bidlot et al., 2005, Fig. 8).

For reference the operational wave model used at the U.S. National Ocean and Atmosphere Administration (NOAA) National

Center for Environmental Prediction (NCEP) does not have this East Pacific bias, thanks to the parameterization of swell attenuation. However, NCEP's model produces significantly larger random errors outside of the tropical ocean, at least for their year 2000 compared to our year 2004 (see Fig. 4 in Tolman, 2003, and compare to our Fig. 2). This better quality of the model, compared to NCEP's, in terms of random errors is consistent with the wave height and period statistics at the buoys (Bidlot et al., 2007a). Although the driving wind fields are different, it is likely that the better agreement is partly due to a better estimation of the magnitude of the wind input and dissipation source terms. Ardhuin et al. (2007) showed that Tolman and Chalikov (1996)'s wind input and dissipation parameterizations (used at NCEP) yield large biases in mean direction at the frequency peak in slanting fetch conditions, which was interpreted as evidence for too weak a forcing in young wave conditions. In this respect, the parameterizations of Bidlot et al. (2005) provide a better fit to short fetch wave directions. The smaller global scale random errors with that latter parameterization thus appear to be related to a more realistic timescale for the wave field evolution.

However, the present model gives some important errors on the wave periods, in particular a large persistent positive bias in the North-East Pacific and Hawaii (Fig. 3).

Clearly the model is not perfect and some further tuning of parameters such as the wind-wave coupling coefficient $\beta_{max}$ could be done. Increasing only $\beta_{max}$ would generally reduce the negative bias for $H_s$ but also reduce the correlation coefficients for $H_s$, and increase the bias on the periods.

### 3.2. Known model deficiencies

The model errors can be traced to three important deficiencies in the parameterization by Bidlot et al. (2005). First and foremost, the parameterization lacks a swell attenuation mechanism (Tolman, 2002). Clear evidence for this is the large latitudinal gradient in biases on $H_s$ and $T_p$ in the Eastern Pacific (Fig. 2). In the present model the waves heights are underestimated where the winds are strongest and overestimated where the winds are weakest. Although this could be attributed to errors in local windsea generation, the fact that this bias is due to swell is confirmed by the analysis of swell fields over large distances using SAR wave mode data from ERS and ENVISAT (Ardhuin et al., 2008a). This effect is also noticeable at mid latitudes, with an overestimation of low wave heights ($H_s < 1$ m) in the North East Atlantic (Fig. 4).

The processes that cause the swell attenuation are not fully elucidated (Ardhuin and Jenkins, 2006; WISE Group, 2007) but they are likely dominated by the damping of waves due to the strong shears at the air–sea interface (Weber and Førland, 1990; Kudryavtsev and Makin, 2004; Ardhuin et al., 2008a), resulting in a wave-driven wind (Grachev et al., 2003). If this is the case, the associated flux of energy is from the wave field back to the atmosphere, and thus irrelevant to the problem of ocean mixing, except for indirect effects through enhanced windsea generation by the wave-driven wind.

Second, the parameterization leads to an overestimation of the wind stress at high winds. For $U_{10} > 30$ m s$^{-1}$, the drag coefficient $C_d$ may exceed 0.04, about a factor 2 larger that the largest esti-

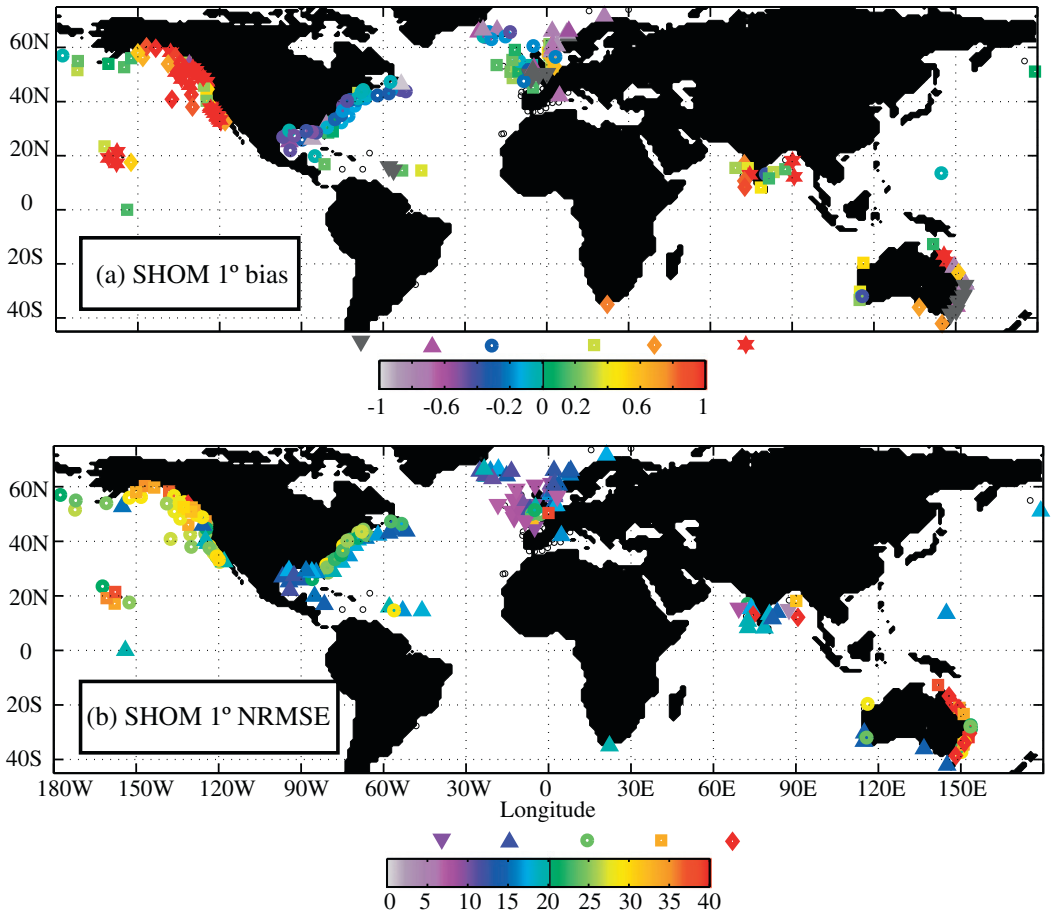


**Fig. 3.** Statistics for the year 2006. (a) Bias in seconds for $T_{m02}$ (most European buoys) or $T_p$ (all other buoys) at *in situ* locations. Symbols ▽, △, ○, □, ◇ and ☆ correspond to values in the ranges $x < -1$., $-1 \leqslant x < -0.5$, $-0.5 \leqslant x < 0$, $0 \leqslant x < 0.5$, $0.5 \leqslant x < 1$, $1 \leqslant x$, respectively. (b) Normalized RMSE for $T_{m02}$ (most European buoys) or $T_p$ (all other buoys). Symbols ▽, △, ○, □, and ◇ correspond to values in the ranges $0 \leqslant x < 10$, $10 \leqslant x < 20$, $20 \leqslant x < 30$, $30 \leqslant x < 40$, $40 \leqslant x$.

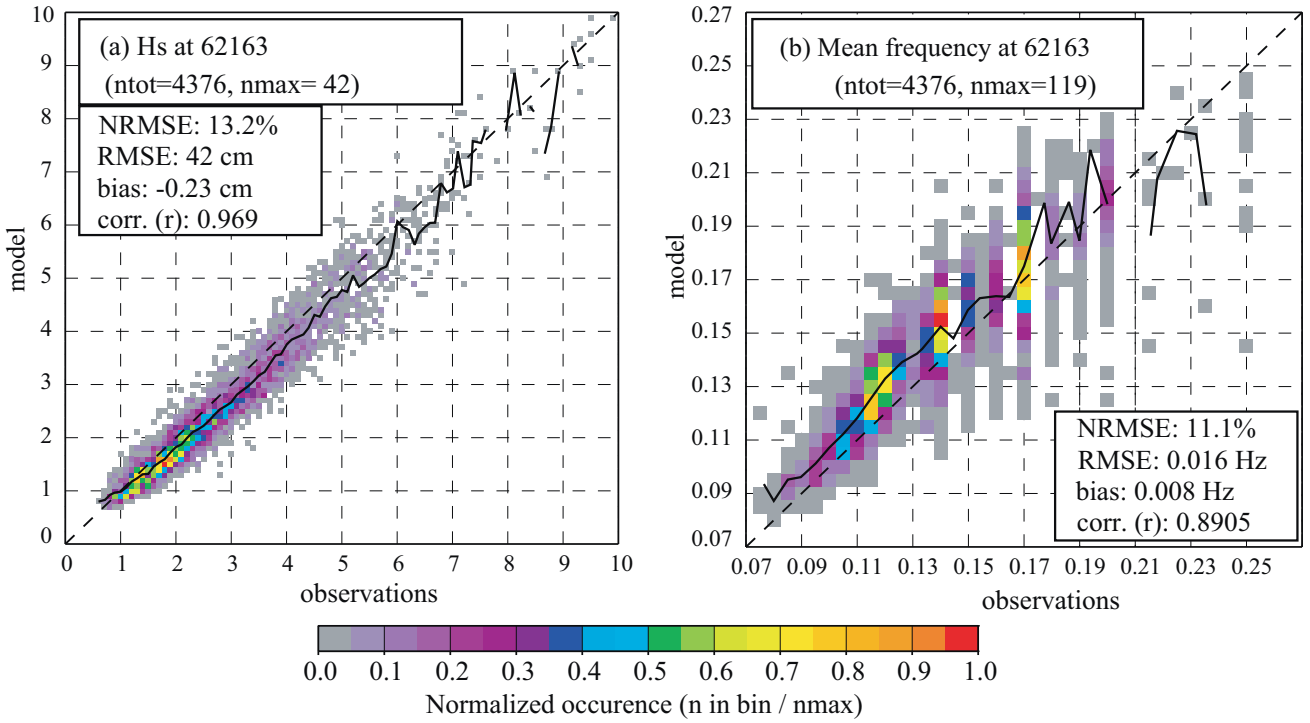


**Fig. 4.** Statistics for the years 2004 and 2005 at buoy 62,163 (47°30′N, 8°24′W, 200 km off the west coast of France). (a) Wave heights and (b) mean periods. The solid line joins the mean observed and modelled value in each observation bin.

mates of $C_d$ based on *in situ* observations (Powell et al., 2003). Although this may lead to local biases in the estimation of atmosphere–wave–ocean energy fluxes, the globally average effect is likely to be small, because these high winds are rare. This will be estimated below by using a correction for the overestimation of $C_d$.

Third, the parameterization of the windsea evolution is unrealistically sensitive to swell, leading to an overestimation of windsea growth in the presence of swell (Ardhuin et al., 2007). Because there is less swell in the Western part of ocean basins, a tuning of the model to average ocean conditions inevitably produces less wind sea on the Western part of ocean basins, and more wind sea where there is more swell, i.e., in the Eastern parts. This likely explains part the zonal gradient in wave height bias with low values from 100 to 2000 km off the U.S. East coast and East Asia. This effect also comes with a moderate underestimation of the high frequency tail, which is mitigated by the use of the $f^{-5}$ diagnostic tail for $f > f_c$.

Finally, the forcing of the model is not perfect either, in particular the ocean currents were neglected here. This is most important where the currents $\mathbf{U}$ are fast relative to either the phase speed $C$ of the waves (in which case refraction and shoaling can be important) or the wind speed $\mathbf{U}_{10}$ (in which case the waves should be generated by the relative wind $\mathbf{U}_{10} - \mathbf{U}$). A preliminary analysis using 0.5° surface current fields from Mercator's PSY3V1 model (Barnier et al., 2006) shows that in the equatorial region, where the yearly average current can exceed 7% of the average wind velocity, currents have a significant impact on $H_s$ (Fig. 5), as already expected by Janssen et al. (2005). Including currents removes most of the small scale structure in the wave height bias over the equatorial current and the north equatorial counter current. In other regions there is an increase of the negative biases, due to the fact that swells are often generated over currents that flow in the wind direction, in particular around the Southern Ocean. Taking into account ocean currents thus reduces the relative wind and the wind-wave growth. In the regions with strong currents, the improvement appears marginal, possibly due to large errors in the current spatial patterns (e.g., Collard et al., 2008).

The parameter settings chosen here are thus a compromise (with a relatively good performance for $H_s$ on the U.S. West coast). A better model has now just been obtained that corrects all of the above defects (Ardhuin et al., 2008a,b). The expansion of the wave parameter database using that model will be fully described in a following paper that will focus on remote sensing applications.

## 4. Wave-related parameters

### 4.1. The surface Stokes drift $\boldsymbol{U}_{ss}$

#### 4.1.1. Stokes drift of non-linear waves

When considering random waves, the Stokes drift is usually estimated from the wave spectrum, assuming that the phases of the wave components are not correlated (Kenyon, 1969). Here we estimate the error due to that assumption using a streamfunction theory (Dean, 1965; Dalrymple, 1974) to order 80 and above, with an explicit calculation of drift velocities along streamlines. We consider the case of deep water waves by choosing $kD = 4.5$, where $k$ is the wavenumber and $D$ is the water depth. In this case, and when the orbital velocity at the crest $U_c$ exceeds 99% of the phase speed $C$, the surface drift may be $q = 1.8$ times the value given by linear theory for the same elevation variance. For these waves $U_s$ exceeds the linear value at the surface over a depth of about 5% times the wave height. However, this speed-up factor $q$ due to the wave nonlinearity drops to 1.06 for $U_c/C = 0.5$, which still corresponds to a very large wave steepness $k H/2 = 0.36$, where $H$ is the wave height. Clearly, very few waves in a random sea state are so steep, and we may expect linear wave theory to provide a reliable estimate of the surface drift, with the exception of the effect of breaking waves.

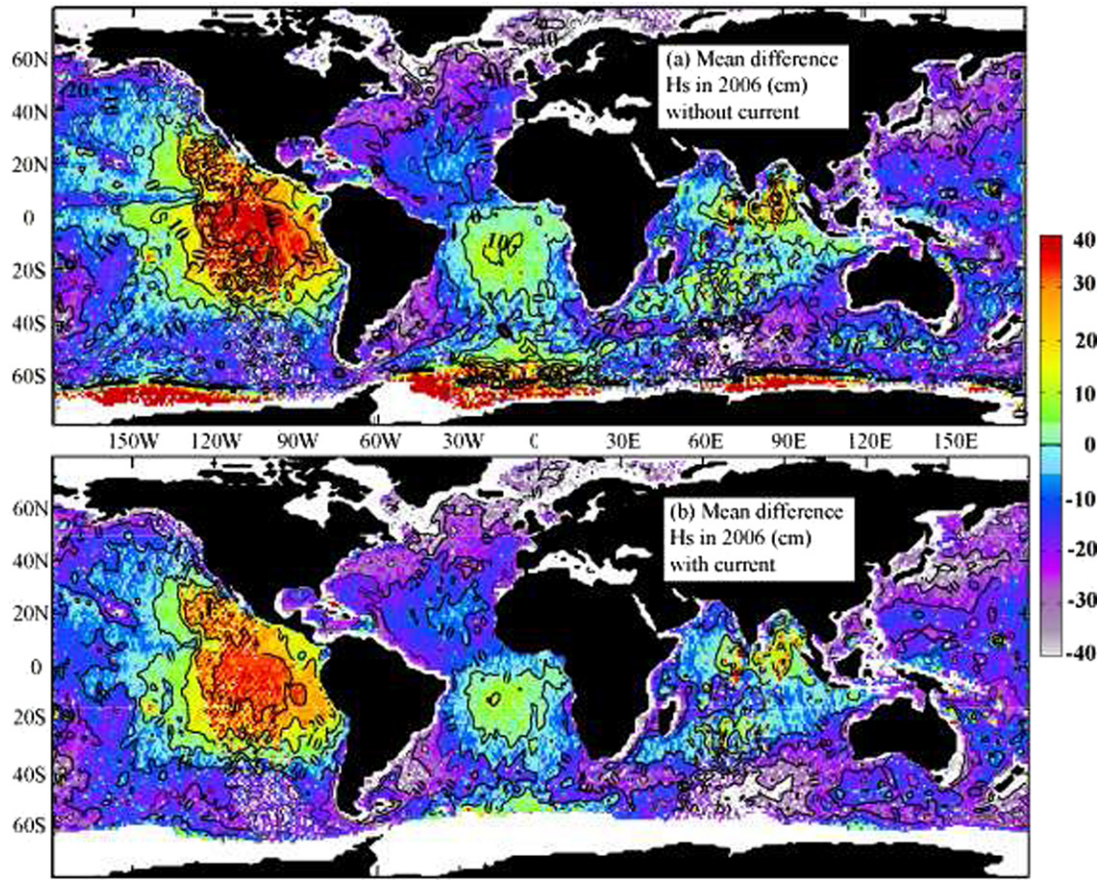


**Fig. 5.** Bias on $H_s$ for 2006, combining data from JASON, ENVISAT and GEOSAT-Follow On (GFO): (a) with the model used here and (b) with the model including forcing by surface currents. See Appendix B for satellite data analysis methods.

*4.1.2. Previous estimations of $U_{ss}$*

We thus use a superposition of linear wave theory results (e.g., Lamb, 1932). In deep water, the surface Stokes drift is

$$\mathbf{U}_{ss} = \frac{2}{g}\int\int \sigma^3 E(f,\theta)\mathbf{u}_\theta \,\mathrm{d}f\,\mathrm{d}\theta, \tag{1}$$

where $\mathbf{u}_\theta = (\cos\theta, \sin\theta)$ is the unit vector in the direction of propagation, and $\sigma = 2\pi f$. This expression has been often used improperly. For example, Kenyon (1969) estimated that the surface drift of fully developed waves could reach 3% of $U_{10}$, but he defined the wave spectrum for that calculation by a non-classical form of the Pierson and Moskowitz (1964) spectrum.

Further, $U_{ss}$ strongly depends on the shape of the high frequency part (the 'tail') of the spectrum. Therefore, these results were reevaluated by Rascle et al. (2006) using the spectrum of Kudryavtsev et al. (1999), which was designed for remote sensing applications and is therefore expected to be more realistic in the high frequency part than the spectrum of Pierson and Moskowitz (1964). It was obtained that $U_{ss}$ can reach a maximum value of 1.2% of the wind speed. This ratio was found to be maximum for high wind speeds (Rascle et al., 2006, Fig. 2b). However, that spectrum lacks the overshoot of the spectral peak (Darbyshire, 1958) and appears less realistic for the long waves.

*4.1.3. Estimation of $U_{ss}$ with a wave model*

Because the wave field is almost never fully developed, and because swells should also contribute to the drift, it is interesting to estimate the Stokes drift for real sea states. The waves are only resolved by the model over the frequency range of the most energetic waves, with a maximum frequency of $f_{max} = 0.72$ Hz. Using data from NDBC buoy 51001, off Hawaii, in the range 0.04–0.4 Hz, the magnitude of $U_{ss}$ was estimated from the frequency spectrum and directional moments. Comparing the results of the 0.5° resolution model to minimize errors due to coastal resolution, we find that $U_{ss}$ for that frequency range is understimated by 17.9% whereas $H_s$ is understimated by only 1.8%. This model error is due to the underestimation of the high frequency tail level in the presence of swell, but also to an overestimation of the directional spread. In fact, if all the waves are taken in the same direction, the bias for $U_{ss}$ is only 10.2%. For the same year, we could also compare to SHOM's directional 0.9 m diameter Datawell buoy off Cap Ferret, with WMO number 62064 and located at 44.7 N and 1.49 W, in 50 m depth. There the underestimation of $H_s$ is 4.2%, and only 10.4% for $U_{ss}$ estimated in the frequency range 0.04–0.54 Hz.

Since higher frequency waves can have a significant contribution to $U_{ss}$, we will extend analytically the spectrum to higher frequencies. Following Phillips (1958), we define the non-dimensional Phillips parameter at $f_{max}$ as

$$\alpha_{Ph}(f_{max},\theta) = \frac{E(f_{max},\theta)\sigma^5}{2\pi g^2}. \tag{2}$$

We then extend the spectrum $E(f,\theta)$ beyond $f_{max}$ by assuming that $\alpha_{Ph}(f,\theta) = \alpha_{Ph}(f_{max},\theta)$ for $f \geqslant f_{max}$, which corresponds to a $f^{-5}$ decrease of $E(f,\theta)$, a prolongation of diagnostic tail already imposed from $f_c$ to $f_{max}$ (see for a discussion of the spectral shape Long and Resio, 2007). The high frequency contribution to $U_{ss}$ is given by

$$\mathbf{U}^+_{ss} = \frac{g}{\pi}\frac{1}{f_{max}}\left[\int_0^{2\pi} \alpha_{Ph}(f_{max},\theta)\mathbf{u}_\theta \,\mathrm{d}\theta\right], \tag{3}$$

which is typically of the order of $0.004U_{10}$ for $f_{max}$ = 0.4 Hz and $0.0025U_{10}$ for $f_{max}$ = 0.72 Hz (Fig. 8).

The consistency of this $f^{-5}$ extension was verified using the method employed by Elfouhaily et al. (1997) who connected the low-frequency spectrum of Donelan et al. (1987) to a high frequency spectrum constrained by a variety of observations. This method was shown to give good results, in the analysis by Elfouhaily et al. (1997), in terms of mean square slope (mss) which is the fourth moment of the frequency spectrum and depends both on the low and on the high frequency parts of the spectrum. Because $U_{ss}$ is close to the third moment of the frequency spectrum, it is expected to behave similarly to the mss, and we applied the method of Elfouhaily et al. (1997) to extend the WWATCH spectrum. The resulting composite spectrum ('WW3ECKV') is obtained by multiplying $E(f)$ by a cut-off factor

$$\exp\left\{-\frac{\Omega}{\sqrt{G}}\left[\sqrt{\frac{k}{k_p}}-1\right]\right\}. \quad (4)$$

Then a high-frequency spectrum is added to the cut-off low frequency spectrum.

With $G$ = 10, one obtains the form used by Elfouhaily et al. (1997), but we found that this cut-off reduces too much the low frequency spectrum in the range $0.2 < f < 0.4$ Hz. Therefore, we increased $G$ to 100. The directional spreading used is given by Eq. 57 in Elfouhaily et al. (1997).

Resulting values of $U_{ss}$ are shown in Fig. 6 and compared to the simple $f^{-5}$ extension of WWATCH ('WW3 + $f^{-5}$'). $U_{ss}$ differ by less than 10% between the three different spectra.

#### 4.1.4. Results

The ratio $U_{ss}/U_{10}$ of the Stokes drift (including the analytical extension) to the wind speed is shown in Fig. 7. This ratio is fairly stable, with an annual mean that varies from 0.8% to 1.5%. Maximum values are found in areas of large wind speeds and/or where waves are fully developed (under the trade winds). $U_{ss}$ is thus expected to be generally twice as large as the surface Ekman current (Rascle et al., 2006; Rascle, 2007).

The variability of the ratio $U_{ss}/U_{10}$ is illustrated in Fig. 8. Values larger than 1.5% correspond to a rapid decrease of the wind while the sea state remains developed.

### 4.2. The Stokes transport $T_S$

The Stokes volume transport $T_S$ is the vertical integral of the Stokes drift. Assuming that the wave field is always fully developed, McWilliams and Restrepo (1999) and Polton et al. (2005) estimated that the mean value of $T_S$ could be as large as 40% of the corresponding Ekman transport $T_E$, depending on the latitude. Rascle et al. (2006) re-evaluated this ratio using the wave spectral shape given by Kudryavtsev et al. (1999), which yields smaller values, around 30% at most for 45° of latitude. The ratio was shown to reach maximum values for high wind speeds. However, waves are never fully developed for large wind speeds. Therefore, we evaluate here the Stokes and Ekman transport from the wave model results. The wind stresses are predicted by the model and are consistent with the results discussed by Bidlot et al. (2007a) using the same parameterizations, and thus consistent with observations. The Stokes transport, being essentially a function of $H_s$ and the mean period $T_{m01}$ should be within 30% of real values, given the wave model errors on $H_s$, $T_{m02}$ and $T_p$. The present estimates are likely more accurate than those of Janssen et al. (2004) who used an earlier parameterization that was giving a large positive bias on the mean period $T_{m02}$, and a 15% bias on first spectral moment $H_s^2/(16T_{m01})$, which would equal $T_S$ if all the waves propagated in the same direction.

Because we define $T_E = \tau/(f\rho_w)$ with $f$ the Coriolis parameter, $T_E$ is much larger than $T_S$ at the Equator where $f$ goes to zero. For

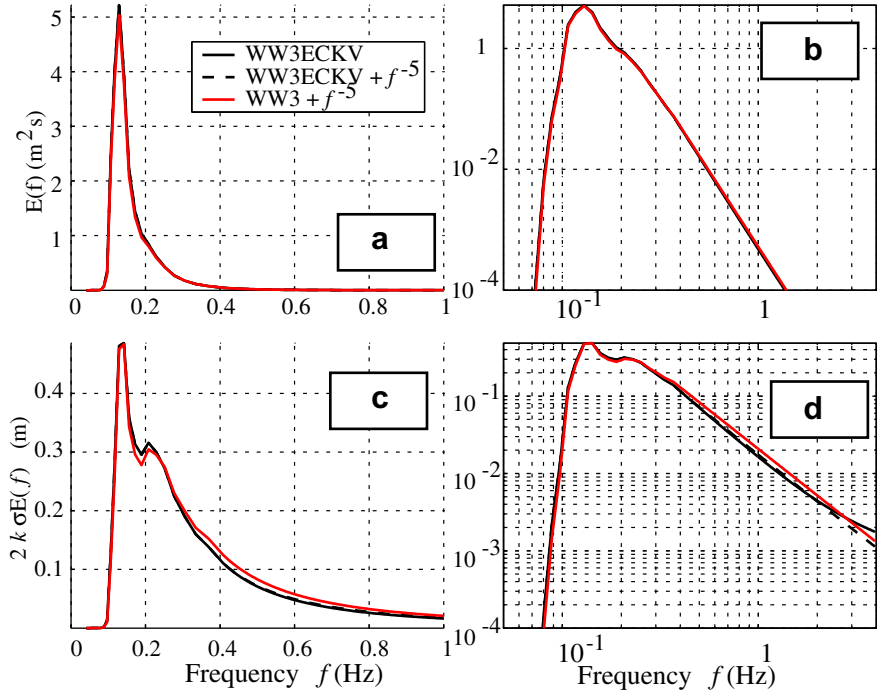


**Fig. 6.** (a, b) Omnidirectional spectrum $E(f) = \int E(f,\theta)\mathrm{d}\theta$. (c, d) Omnidirectional spectrum of the third spectral moment $2/g \int \sigma^3 \cos(\theta) E(f,\theta)\mathrm{d}\theta$, as function of the frequency (this is the spectrum of $U_{ss}$ in the case of unidirectional waves). Left panels are linear plots while rights panels are log–log plots. Three different spectra are used: the WWATCH spectrum, cut at $f_{max}$ and extended with an $f^{-5}$ tail ('WW3 + $f^{-5}$', red line), our composite spectrum connecting WWATCH to a high frequency tail as in Elfouhaily et al. (1997) ('WW3ECKV', solid black line) and our composite spectrum cut at $f_{max}$, and extended with a $f^{-5}$ tail ('WW3ECKV + $f^{-5}$', dashed black line). In the particular realization shown, $f_{max}$ is set to 0.4 Hz, the wind is set to $U_{10}$ = 10 m s$^{-1}$ and the waves are fully developed. $U_{ss}$ reaches 12.2 cm s$^{-1}$ with 'WW3 + $f^{-5}$' whereas it reaches 11.5 cm s$^{-1}$ with 'WW3ETKV' and 'WW3ETKV + $f^{-5}$'.

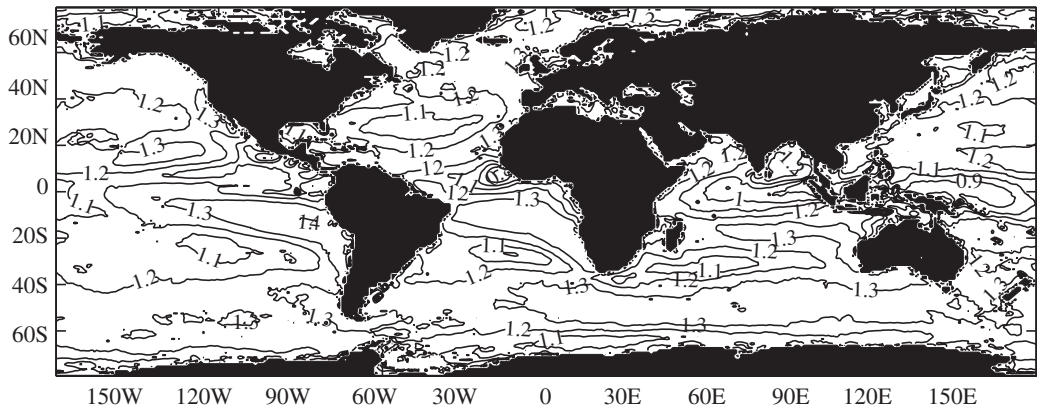


**Fig. 7.** Mean values of the ratio of the surface Stokes drift and wind speed $\langle U_{ss}/U_{10}\rangle$, over the year 2004, in percentage. Contours are every 0.1%.

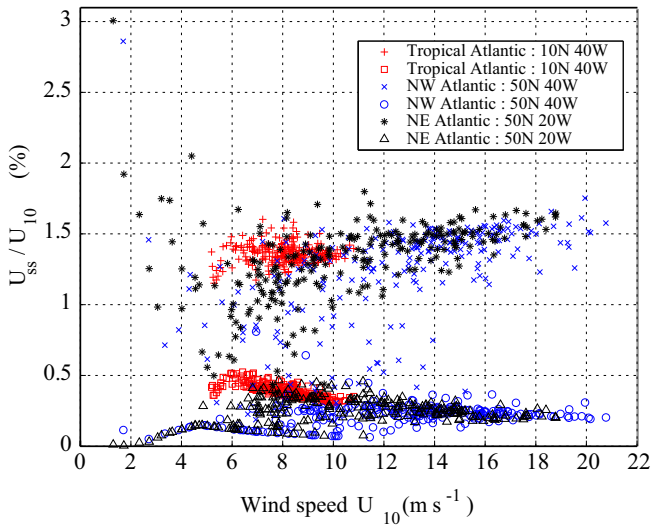


**Fig. 8.** Ratio of the surface Stokes drift $U_{ss}$ to the wind speed $U_{10}$ at 10 m, in percentage, as function of the wind speed $U_{10}$, at three locations. Each symbol corresponds to one wave model output, every 3 h, for January 2004. Symbols ☆, + and × denote the full Stokes drift $U_{ss}$ while the open symbols denote the contribution of the high frequency extension to the Stokes drift $U_{ss}^{+}$.

well-developed windseas, more commonly found in the Eastern part of ocean basins, $T_S$ can indeed be as large as 20–35% of $T_E$ for moderate to high wind speeds, respectively, as shown on Fig. 9. In areas with high swells, $T_S$ can actually be of the order of $T_E$ on average, as found under the atmospheric convergence zones at 30°N and 30°S where $T_S/T_E$ can reach 60%.

Although this occurs in areas that cover a very small part of the world ocean, this Stokes transport should be locally very significant for material tracer evolution (larvae, plankton, contaminants). It is also expected that the Stokes–Coriolis force should have a significant effect on the mixed layer dynamics in these areas, while it is generally weaker over most regions, especially on the western part of the ocean basins (see also Rascle, 2007, Fig. 3.9, for a reanalysis of the LOTUS field experiment).

### 4.3. The roughness length $z_0$

#### 4.3.1. Values of $z_0$ and global estimations

The roughness length $z_0$ is physically understood as the scale of the breaking waves and related eddies that are responsible for the high mixing levels close to the surface (Kitaigorodskii, 1994; Melville et al., 2002). It has been shown by Craig and Banner (1994) and by Mellor and Blumberg (2004) that this length scale is more important in terms of mixing than the amount of TKE injected by breaking waves. That length scale has been related to the significant wave height $H_s$ (Terray et al., 1996). Terray et al. (2000) proposed that

$$z_0 = 1.6H_s, \tag{5}$$

and verified that it was consistent with their Eulerian measurements (see also Rascle et al., 2006). Given that swells (waves not related to the local wind) generally have small orbital velocities compared to their phase speeds, they do not break (Miche, 1944). Waves at the spectral peak in fully developed conditions also break very infrequently (Banner et al., 2000). We may thus replace $H_s$ by the windsea wave height ($H_{swg}$). This separation is performed in the wave spectrum based on the sign of the wind generation function, namely

$$H_{swg} = 4\left(\int_{S_{in}(k)>0} E(k)\mathrm{d}k\right)^{1/2}, \tag{6}$$

where $E(k)$ is the variance of the surface elevation for a given wavenumber $k$ and $S_{in}$ is the energy input term in the wave energy equation. For developed waves a large fraction of the energy corresponds to waves propagating slightly faster than the wind and for which $S_{in} \leqslant 0$. Our definition (6) thus yields a smaller height than the usual windsea partition $H_{sws}$ based on the analysis of local maxima in the spectrum (e.g., Hanson and Phillips, 2001). As a consequence, for a young windsea without swell, $H_{swg} = H_s$, whereas for a fully developed windsea, $H_{swg} < H_s$, the difference being typically of the order of 10–20%. Using $H_{swg}$ instead of $H_s$ or $H_{sws}$ is also consistent with the estimate $z_0/H_s \simeq 0.6$ by Soloviev and Lukas (2003) based on measurements in tropical sea states, for mature waves. This definition will be perfected when reliable breaking statistics can be estimated from the wave spectral shape, making it less sensitive to the faster fluctuations in wind speed.

One should be aware of a remaining discrepancy with the data of Gemmrich and Farmer (2004) who rather suggest $z_0/H_s \simeq 0.25$. The difference in these estimates is possibly due to variations in the method of averaging, Eulerian in the case of Terray et al. (1996), and surface following in the case of Gemmrich and Farmer (2004).

From a mixing perspective, $H_{swg}$ gives a scale of the minimum MLD, and thus the extremes of $H_{swg}$ should be more closely related to the MLD than the mean. These maxima are largely controlled by extreme events, in particular tropical and extra-tropical cyclones. The tracks of several storms, including hurricane Ivan in the Gulf

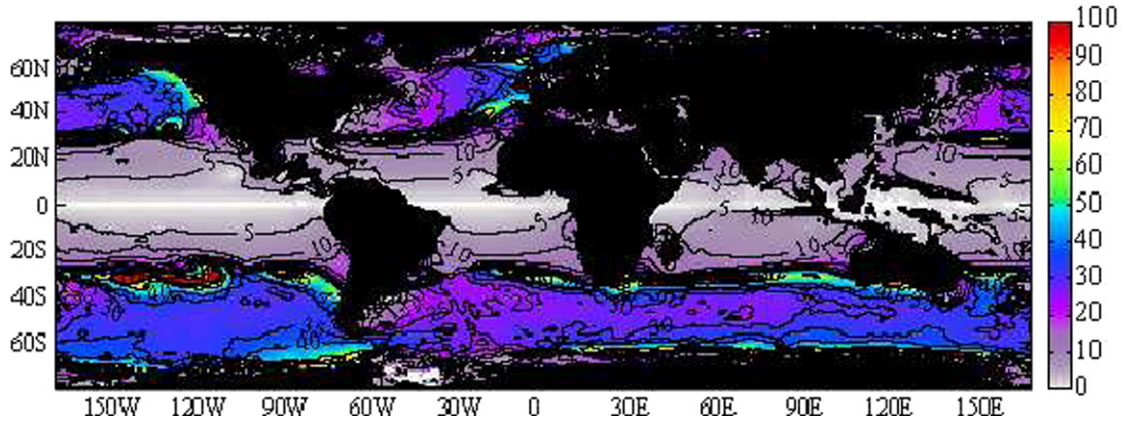


**Fig. 9.** Ratio of the Stokes transport $T_S$ to the Ekman transport $T_E = w_{\star}^2/f$, in percentage. Values shown are ratios of the vector averages $\langle T_S \rangle / \langle T_E \rangle$, taken over the year 2004. Contours are every 5% up to 40% and every 20% above.

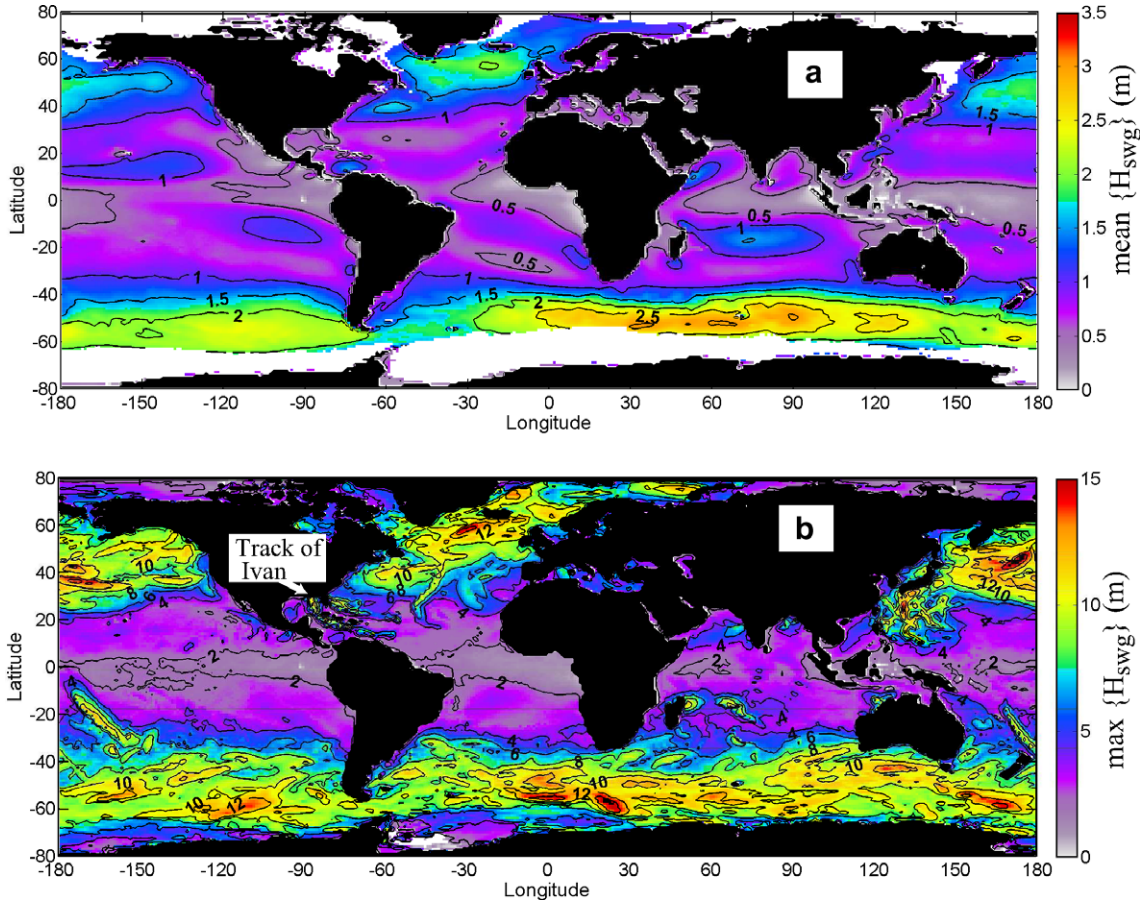


**Fig. 10.** Significant wave height of the windsea, $H_{swg}$ (m), as estimated from the wave model using Eq. (6). Values shown are (a) mean values of $H_{swg}$ over the year 2004 (contours every 0.5 m), and (b) maximum values of $H_{swg}$ over the same year (contours every 2 m).

of Mexico, are clearly visible in Fig. 10b, whereas they do not appear in the mean values. It should be noted that the resolution of the present global model is insufficient to properly resolve in space and time the wind and wave fields of tropical cyclones. In the case of hurricane Ivan, the maximum value of $H_s$ given by the 1° global model is only 12.5 m, while 15 m has been measured by a buoy Wang et al., 2005. This underestimation is only 1 m when observations are averaged over 3 h.

Because many ocean circulation models use daily mean fluxes, we recommend the use of daily maxima of $H_{swg}$ in such models. Of course, since this parameter is most important for the diurnal cycle, it would be logical to also use a higher frequency forcing.

*4.3.2. Simplistic parameterizations*

Mellor and Blumberg (2004) have related the wave height $H_s$ to the friction velocity $u_{\star}$, using an approximate equation for the wave height as a function of the wind stress and wave age

$$H_s = \frac{\beta}{0.85}\frac{w_{\star}^2}{g}, \quad \beta = 665\left(\frac{C_p}{u_{\star}}\right)^{1.5}, \tag{7}$$

where $C_p/u_{\star}$ is the wave age, i.e., the ratio of the phase speed of the dominant waves to the atmospheric friction velocity. $w_{\star}$ is the waterside friction velocity, related to the atmospheric friction velocity with

$$r = \frac{w_{\star}}{u_{\star}} = (\rho_a/\rho_w)^{1/2} \simeq 1/28, \tag{8}$$

where $\rho_a$ and $\rho_w$ are the density of air and water, respectively.

Note that Mellor and Blumberg (2004) used the definition of the mixing length $l = \kappa \max(z'_0, |z|)$, with the corresponding roughness length $z'_0 \simeq 0.85 H_s$ (Terray et al., 2000). As discussed in Rascle et al. (2006), this estimation is not reliable and the definition $l = \kappa(z_0 + |z|)$ is preferable, with the corresponding roughness length being $z_0 \simeq 1.6 H_s$. Because of these different definitions of $z_0$, we limit here our discussion to the values of $H_s$.

For a wave age of $C_p/u_{\star} = 30$, i.e., fully developed waves, Eq. (7) gives

$$H_s = \frac{\beta}{0.85}\frac{w_{\star}^2}{g}, \quad \beta = 1 \times 10^5. \tag{9}$$

Estimations of $z_0$ by Stacey (1999), from velocity profiles observations in a Canadian fjord, gave an even larger value $\beta = 2 \times 10^5$, although the waves were quite young.

Based on this evidence, Mellor and Blumberg (2004) used values of $\beta$ between $1 \times 10^5$ and $2 \times 10^5$. Their sensitivity study suggests that Eq. (9) can be used to parameterize the wave height as function of the local wind. However, waves are almost never fully developed, and the comparison of the parameterization (9) of the windsea wave height and the calculation from the wave model, using Eq. (6), shows a large discrepancy at mid-latitudes, while the agreement is acceptable at low latitudes (Fig. 11).

The wave age $C_p/u_{\star}$ is obviously missing in a direct parameterization of the wind-wave height from the wind such as Eq. (9). Waves are generally fully developed under weak winds and are often quite young under strong winds (Fig. 11). Although we recommend using wave parameters from a wave model, we nevertheless propose here a better approximation of the wind-wave height as a function of the wind, for those who really do not want to use a wave model. This approximation supposes that the wave age is a function of the wind speed

$$\frac{C_p}{u_{\star}} = 30 \tan h\left(\frac{2u_{\star \mathrm{ref}}}{u_{\star}}\right), \tag{10}$$

where $u_{\star \mathrm{ref}}$ is a typical friction velocity above which the wave growth is limited by the fetch or the duration of the wind (see Fig. 13a). Here we set $u_{\star \mathrm{ref}} = 0.3$ m s$^{-1}$. The wave height is then given by the wind stress with

$$H_s = \frac{\beta}{0.85}\frac{w_{\star}^2}{g}, \quad \beta = 665[30 \tan h(u_{\star \mathrm{ref}}/u_{\star})]^{1.5}. \tag{11}$$

This estimation corrects the bias in the mean significant windsea wave height $\langle H_{swg} \rangle$ (Fig. 11).

For average wave-induced mixing, Eq. (11) may be used as a rough parameterization of the wave-breaking effect on the mixing, for instance for application to an OGCM. Eq. (9) should be useful to give an upper bound for the wave-induced mixing. However, the use of a wave model in addition to the ocean circulation model is by far preferable to such simple climatological parameters because the spatial and temporal variability of extreme events would be better represented.

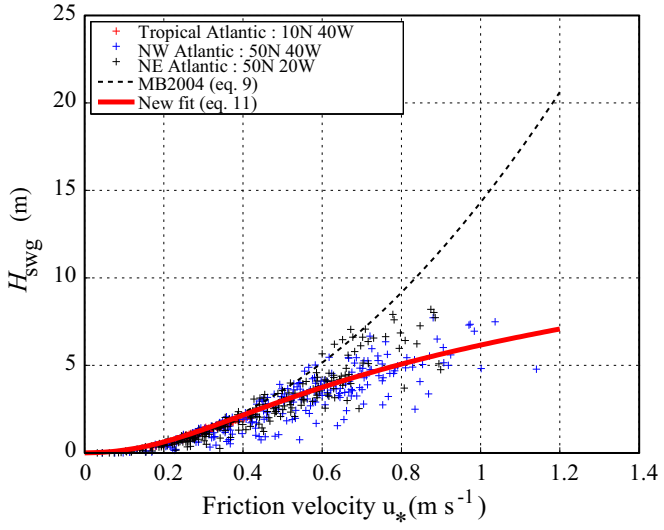


**Fig. 11.** Significant windsea wave height $H_{swg}$ as a function of the air-side friction velocity $u_{\star}$. Each symbol corresponds to one wave model output, every 3 h, for January 2004. Three locations of the North Atlantic are shown, one from the Tropical Atlantic, one from the North-East Atlantic and one from the North-West Atlantic. Also shown is the wave height as inferred from (9), which supposes full development. At low wind speed, the waves are often close to full development. However, for large wind speeds at mid-latitudes, waves are less developed, especially in the west part of the oceans. Therefore, we also show the wave height obtained by supposing that the wave age is a function of the wind speed via (10) and (11).

### 4.4. Fluxes of turbulent kinetic energy

#### 4.4.1. Previous estimates of $\Phi_{oc}$

As waves break they give up part of their momentum $M^w = \rho_w T_S$ and energy $E = \rho_w g H_s^2/16$, to the mean current and turbulence, respectively. Because the ratio of the losses of momentum and energy is the phase speed of the breaking wave, while the corresponding ratio for the current is the generally much smaller current velocity, one may neglect the gain of kinetic energy by the current and consider that all the wave energy lost by breaking is converted to TKE. Indeed, the mean phase velocity of breaking waves $\overline{C}$ was estimated between 0.05 and $0.12 \times U_{10}$ by Gemmrich et al. (1994), while the wind driven current is typically of the order of $0.005 \times U_{10}$ at large scales (Rascle et al., 2006). Janssen et al. (2004) gave a mean value $\overline{C} = 5.2 u_{\star} \simeq 0.15 U_{10}$, with large regional fluctuations. That latter estimation was performed with a numerical wave model, an approach that we follow here. Preliminary calculation reported in Rascle (2007) were up to a factor of two larger due to a numerical error.

Due to the variability of the wave field, it is convenient to normalize the flux $\Phi_{oc}$ by the air density $\rho_a$ and air-side friction velocity $u_{\star}$, or the water density $\rho_w$ and water-side friction velocity $w_{\star} = r u_{\star}$. In that latter form, $\Phi_{oc} = \rho_w \alpha_{CB} w_{\star}^3$ is determined by the Craig and Banner (1994) parameter $\alpha_{CB}$. Measurements of $\alpha_{CB}$ are very difficult because most of the TKE generated by the waves is dissipated very near the surface, where measurements are made extremely difficult due to the moving surface and the presence of bubbles entrained by breaking waves (e.g., Gemmrich and Farmer, 2004). Because the atmosphere to wave energy flux $\Phi_{aw}$ should be within a few percent of $\Phi_{oc}$ (Donelan, 1999; Janssen et al., 2004), it is convenient to use the better known $\Phi_{aw}$ and its spectral distribution. Terray et al. (1996) calculated $\Phi_{oc}$ using empirical expressions for the energy input from wind to waves, $S_{in}(f, \theta)$, given by Donelan et al. (1987), and integrated over a large variety of observed wave energy spectra to give $\Phi_{aw}$. They obtained values of $\alpha_{CB}$ between 50 and 150, depending on the wave age (Terray et al., 1996, Fig. 8). The monthly mean estimate $0 < \overline{C}/u_{\star} < 6$ by Janssen et al. (2004), Fig. 14, for most regions of the world ocean, is consistent with $0 < \alpha_{CB} < 170$ because

$$\alpha_{oc} = \overline{C}/u_{\star} = r\alpha_{CB}. \quad (12)$$

Nevertheless, it should be noted that the wind-wave growth term of Donelan et al. (1987) was later revised by Donelan, 1990, with the dimensionless growth factor increased from 0.19 to 0.28. We thus expect that a proportional increase applies to the $\Phi_{oc}$ estimated by Terray et al. (1996).

*4.4.2. Values of $\Phi_{oc}$ and global atmosphere–ocean energy fluxes*

The wave growth factor used by Janssen et al. (2004) and in the present paper is a function of the wave age and wave-supported stress. Our best estimate of the monthly mean values of $\alpha_{CB}$ is generally consistent with the results of Janssen et al. (2004). Minor differences are likely due to a different parameterization of the dissipation and definition of the prognostic range in the wave model, as changed by Bidlot et al. (2005), and our use of a larger frequency range, with $f_{max}$ = 0.72 Hz. In particular, our estimates of $u_{\star}$, are identical to those of Bidlot et al. (2005). The present values of $u_{\star}$ agree with the relatively young waves measured during HEXOS (Bidlot et al., 2007a), but careful and more general validation of $u_{\star}$ is needed, as was done by Bonekamp et al. (2002) with the old version of ECWAM.

It is suspected that $u_{\star}$ is still overestimated for $U_{10} > 25$ m s$^{-1}$. Simulations of the 2004 hurricane Ivan with the present model ran at a resolution of 0.1° and using wind fields from NOAA's Hurricane Research Division (Powell and Houston, 1998) produces drag coefficients $C_d u_{\star}^2/U_{10}$ that can be as large as 0.004, while field observations and inverse ocean modelling suggest maximum values between 0.002 and 0.003 (Powell et al., 2003; Jarosz et al., 2007). In order to evaluate the effect of this overestimation for high winds, we have corrected the fluxes $\Phi_{aw}$ and $\Phi_{oc}$ by assuming unchanged values of $\alpha_{aw} = \Phi_{aw}/(\rho_a u_{\star}^3)$, and adjusting $u_{\star}$ to limit $C_d$ to a maximum value of 0.002. This correction has a very limited impact on yearly mean values.

We further find that the global mean flux of TKE from waves to the ocean is 0.20 W m$^{-2}$, with mean values close to 0.05 in the tropics and up to 0.9 W m$^{-2}$ at mid-latitudes. Integrated over the ocean this gives a total atmosphere to wave flux of 70 TW, out of which 2.4 TW are radiated to the shores and 68 TW are available for ocean mixing. In these 68 TW, there are of the order of $\langle \rho_a u_{\star} U_{ss} \rangle$ = 6 TW of TKE produced by the straining turbulence due to the Stokes drift (Ardhuin and Jenkins, 2006, the actual number depends on the stratification, see also Kantha and Clayson, 2004), which may fuel Langmuir circulation. A sketch of the atmosphere–waves–ocean energy budget is presented in Fig. 12.

The reader may compare our estimate to the much smaller number given by Wunsch and Ferrari (2003, their Fig. 5). This energy is eventually converted to heat. Although this flux of energy is very small in the global ocean heat budget, it may still have a significant effect in long term climate simulations. More importantly this flux can locally exceed 50 W m$^{-2}$, in hurricanes of category 3 and above. Because the effective phase speed $\overline{C}$ is of the order of 10–15% of $U_{10}$ in hurricane conditions, this dissipative heating of the ocean amounts to only 10–15% of the atmospheric dissipative heating discussed by Bister and Emanuel (1998). To our knowledge this term has not yet been included in coupled ocean–wave–atmosphere models of hurricanes, but given its relatively small magnitude, it is unlikely to have a major impact on hurricane dynamics.

*4.4.3. Simplistic parameterizations*

Again, we do not advise parameterizing the wave field from the wind only. We nevertheless reconsider the simple parameterizations of $\Phi_{oc}$, that may provide useful order of magnitudes. Fitting the flux data shown in Terray et al. (1996, their Fig. 8), Mellor and Blumberg (2004) proposed the expression

$$\alpha_{CB} = 15 \frac{C_p}{u_{\star}} \exp\left[-\left(0.04 \frac{C_p}{u_{\star}}\right)^4\right]. \quad (13)$$

As that expression does not fit the WWATCH calculation very well (Fig. 13b), we propose the following correction to account for the parameterization used in WWATCH

$$\alpha_{CB} = P\left(\frac{C_p}{u_{\star}}\right). \quad (14)$$

$P$ is a third-order polynomial to fit $\alpha_{CB}$ as a function of the wave age

$$P(x) = -0.0135x^3 + 0.41x^2 + 3x. \quad (15)$$

This fit provides reasonable values compared to $\alpha_{CB}$ calculated with WWATCH (Fig. 13b).

Janssen et al. (2004) further highlighted the spatial distribution of the parameter $\alpha_{CB}$, which exhibits a strong latitude dependency, because the wave field is often less developed at mid-latitudes (see their Fig. 14). Our result show the same pattern but with a weaker

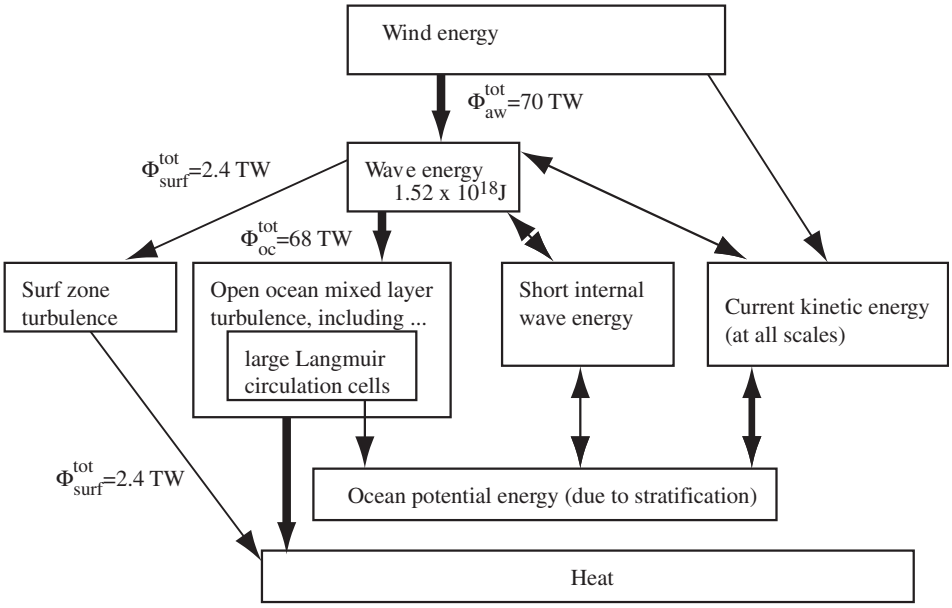


**Fig. 12.** Wave-related energy budget between the atmosphere and ocean.

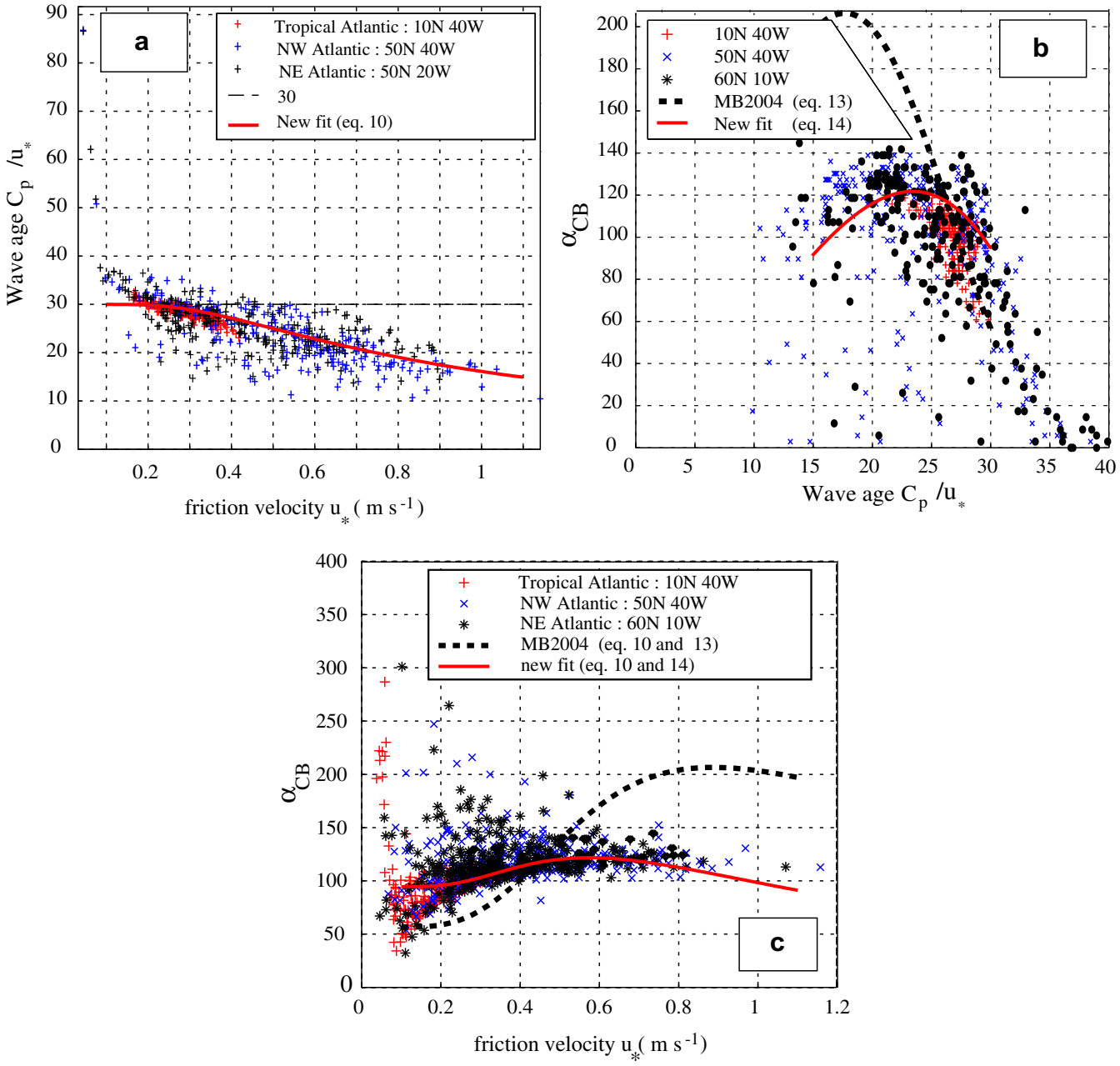


**Fig. 13.** (a) Wave age $C_p/u_{\star}$ as function of the friction velocity $u_{\star}$, compared to Eq. (10), for the month of January 2004. (b) Relationship between the Craig–Banner parameter $\alpha_{CB}$ and the wave age, compared to the parameterization (13) Terray et al., 1996; Mellor and Blumberg, 2004 and to our corrected parameterization (14). (c) Daily mean Craig–Banner parameter $\langle\alpha_{CB}\rangle_{1day} = \langle\Phi_{oc}\rangle_{1day}/(\langle W_{\star}^2\rangle_{1day})^{3/2}$, as a function of the waterside friction velocity $u_{\star}$, for the entire year 2004. The 1 day subscript means that the average is taken over one day. Each symbol thus corresponds to a one-day average using the cumulated energy flux and momentum flux. Also shown are the parameters $\alpha_{CB}$ calculated by supposing that the wave age is a function of the wind speed (Eq. (10)), and that $\alpha_{CB}$ is a function of the wave age according to Mellor and Blumberg (2004) (Eq. (13), dashed line) or according to our corrected formulation (Eq. (14), solid lines). Three locations of the North Atlantic are shown, one from the Tropical Atlantic, one from the North-East Atlantic and one from the North-West Atlantic.

gradient (not shown), probably due to the fact that we take into account the shorter waves ($f_{max} = 0.72$ Hz instead of 0.4 Hz) that dominate the tropical windseas and were absent in that earlier work.

Once again, the wave age is often correlated with the wind stress (Fig. 13a), leading to a correlation between the parameter $\alpha_{oc}$ and the wind stress. Rather than supposing the parameter $\alpha_{oc}$ constant, a simple parameterization of $\alpha_{oc}$ as a function of the wind stress would be more accurate. Of course, we again insist that using a wave model to derive these parameters would be better, since such an empirical fit cannot reproduce the full variability due to the wave field. If, as in the previous section, one supposes that the wave-age depends on the wind stress via (10), then one could use (14) to estimate $\alpha_{oc}$ directly from the wind stress. It is shown in Fig. 13c that such an estimation fits the WWATCH calculations reasonably well. On the contrary the formulation (13) largely overestimates $\alpha_{oc}$ at large wind speeds (Fig. 13c).

## 5. Impact of the wave-related parameters on the mixed layer depth

In this section, we perform a sensitivity study of the impact of the previously discussed parameters on the MLD. We use the sim-

ple one-dimensional model of Noh (1996). In the absence of stratification, this model is equivalent to the model of Craig and Banner (1994), which takes into account the wave-induced near-surface mixing with a surface flux of TKE $\Phi_{oc}$ and a large roughness length $z_0$. The model of Noh (1996) extends to stratified conditions in a way similar to the model of Gaspar et al. (1990). Their main common feature is that the buoyant length scale $l_b = q/N$, where $q^2/2$ is the TKE and $N$ is the Brunt-Väisälä frequency, gives an upper bound on the mixing length $l$, in particular for strong stratifications. The main difference with the model of Mellor and Yamada (1982) is that the flux Richardson number is replaced by a turbulent Richardson number, which is more convenient in the ocean surface layer where the production of turbulence by the mean current shear is not the dominant source of TKE (Noh, 1996).

The model of Noh (1996) was run with a time step $dt = 10$ s. It is shown in Fig. 14 that the diurnal MLD obtained with this model in the presence of both wind- and wave-induced mixing and a stabilizing buoyancy flux strongly depends on the sea state parameters. This is also the case for the rate of thermocline erosion without buoyancy flux (Fig. 15).

Upper ocean stratification is clearly sensitive to the sea state parameters $z_0$ and $\Phi_{oc}$. This result is unambiguous for shallow mixed layers. An estimation of the depths reached by the downward flux of the TKE is around a few times $z_0$ (see Craig and Banner, 1994, their Eq. (27)). The downward flux of TKE due to surface waves is thus expected to be important for depths of the order of a few tens of meters, in particular in the presence of neutral or stabilizing buoyancy fluxes, such as in the Arabian Sea or the Southern Ocean during the southern hemisphere summer.

At greater depths, mixing is probably dominated by other processes. Some of them are related to the sea state, like the Langmuir circulation, while other phenomena are not, such as the current shear at the thermocline due to inertial oscillations (Li et al., 1995) or the internal waves. The impact of surface waves on ocean mixing at greater depth is unclear, as it is likely overwhelmed by other phenomena. More sophisticated models are needed to compare the intensity and the depths that the different sources of turbulence can reach (e.g., Sullivan et al., 2007).

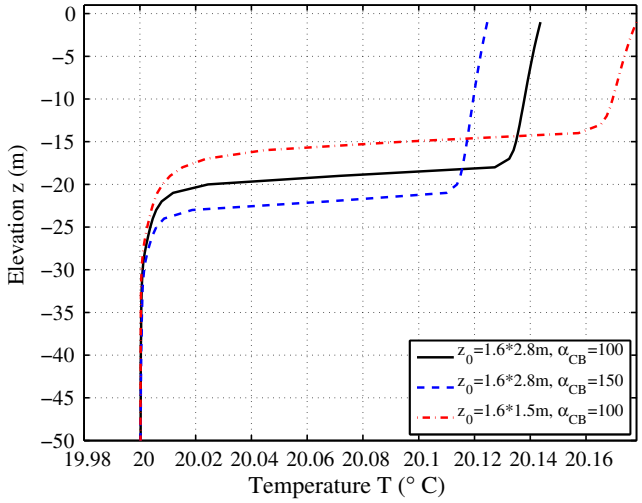


**Fig. 14.** Impact of the wave development on the diurnal mixed layer depth, as inferred from a simple TKE model Noh, 1996;Noh and Kim, 1999. The temperature profile is calculated from an initially uniform temperature of $T = 20$ °C, after 6 h of stabilizing buoyancy flux of 500 W m$^{-2}$ and of mixing due to a wind of 10 m s$^{-1}$ and its associated windsea. Solid line is for fully developed waves ($H_s = 2.8$ m) while dash-dotted line is for a limiting fetch of 100 km ($H_s = 1.5$ m). Those are typical on a continental shelf during onshore and offshore wind events. More developed waves provide more intense near-surface mixing, which creates a deeper diurnal mixed layer. Also shown is the impact of variations of the TKE flux: dashed line is with a parameter $\alpha_{CB}$ 50% larger.

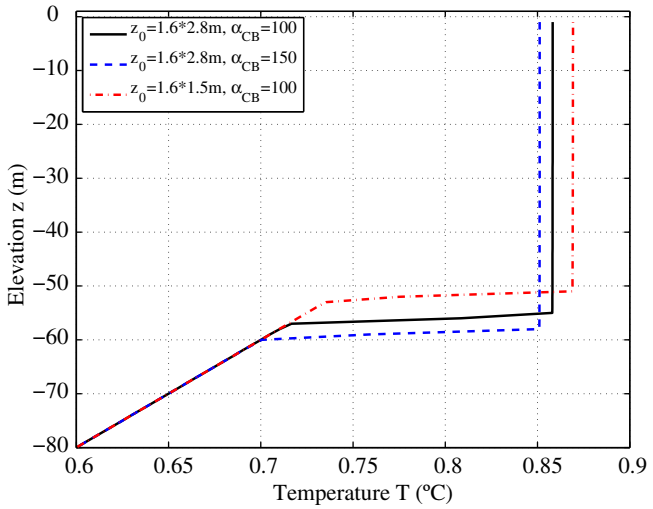


**Fig. 15.** Impact of the wave development on the deepening of the mixed layer. The initial temperature is calculated from an initial profile $T = 1 + 0.005z$, where $z \leqslant 0$, after 120 h of erosion of the stratification without any buoyancy flux but with mixing due to a wind of 10 m s$^{-1}$ and its associated windsea. Solid line is for fully developed waves ($H_s = 2.8$ m) while dash-dotted line is for a limiting fetch of 100 km ($H_s = 1.5$ m). Also shown is the impact of variations of the TKE flux: dashed line is with a parameter $\alpha_{CB}$ 50% larger. It is shown that the different stages of wave development may have an impact on the thermocline erosion: more intense mixing provides faster erosion.

Similarly, the TKE dissipation measurements used to build simple TKE models of the near-surface wave-induced mixing were made at quite shallow depths (e.g., Terray et al., 2000). Deeper measurements are clearly needed.

## 6. Conclusion and future improvements of the database

Ocean surface mixing and drift are functions of the surface Stokes drift $U_{ss}$, volume Stokes transport $T_S$, a wave breaking height scale $H_{swg}$, and the flux of energy from waves to ocean turbulent kinetic energy $\Phi_{oc}$. Here we describe a global database of these parameters that covers the years 2004–2007, estimated from a well-validated numerical wave model for the open ocean. Compared to previous estimates of these parameters, the present work has the advantage of being consistent with the known physical processes that regulate the wave field and the air–sea fluxes, and also consistent with a very large number of observations of wave parameters using *in situ* measurements and satellite remote sensing.

Our estimates may differ significantly from previous estimates. In particular, we find that the global TKE flux $\Phi_{oc}$ is 68 TW and the mean Stokes volume transport, is typically of the order of 30% of the Ekman transport, with values larger on the Eastern part of ocean basins, and very strong values in areas with large swells, just outside of the mid-latitudes storm tracks. We also have refined our previous estimates of the surface Stokes drift $U_{ss}$ by using a better treatment of the implicit high frequency part of the wave spectrum. In the open ocean, $U_{ss}$ is of the order of 1.5% of the wind speed $U_{10}$.

The model described here is known to overestimate swell heights, which should have a minimal impact on the air–sea flux parameters, and underestimate windsea wave heights. The database presented here has already been doubled and extended in time using a new parameterization that takes into account the damping of waves by the wind (Ardhuin et al., 2008a), with better

results obtained for significant wave heights, peak and mean periods and energy levels in the high frequency tail. Validation of that new model in terms of wind stress and Stokes drift and transport is under way, and will be reported in a following paper. In the future, the database will be extended to include other wave-related parameters of interest to other geophysical applications. These include parameters relevant for remote sensing applications, momentum fluxes in and out of the wave field to allow a modelling of the full wave-current coupling (Ardhuin et al., 2008c), and microseism generation forces (e.g., Kedar et al., 2008).

## Acknowledgements

This research would not have been possible without the wind and ice fields provided by ECMWF and Meteo-France, the surface current fields provided by Mercator-Ocean (http://www.mercator-ocean.eu), the satellite altimeter data provided by ESA and CNES, and the many *in situ* observations acquired by all contributors to the JCOMM (WMO-IOC) exchange program. The quality of the present model and feasibility of our research owes much to the very kind help from H.L. Tolman (NOAA/NCEP), P.A.E.M. Janssen and Jean Bidlot (ECMWF), and Bertrand Chapron and Jean-François Piolle (Ifremer). The model configuration was initially built by F. Collard who designed the tool to produce the subgrid island mask from a coastline database. N.R. acknowledges the support of a CNRS-DGA doctoral research grant. This work was partially funded by the Groupe Mission Mercator-Coriolis.

## Appendix A. Database variables, formats and organization

The database is organized by model configuration, i.e., 'GLOBAL', described here or GASCOGNE, which is a 0.1° resolution model of the Bay of Biscay, but also 'GLOBAL_05_NOC' which is a 0.5° global model using a new parameterization. For each model configuration the results are grouped by year, from 2003 to 2008. Necessary model input files are also provided, except for wind, ice and current forcing which are a property of ECMWF and Mercator.

For each year, two types of variables have been computed and stored. The first are spectra at preselected locations (buoys and other places of interest). These spectra are contained in files named after the WMO buoy number, or the geographical position. The spectra were further processed to integrated bulk parameters such as the wave height $H_s$ and several mean periods.

The second type of output are scalar (or 2 component vector) variables. These are estimated over the entire grid at run time. The gridded variables listed in Table A.1 have been stored.

The energy fluxes $\Phi_{oc}$ and $\Phi_{aw}$ in Watts per meter squared are obtained using

$$\Phi_{oc} = \rho_a \alpha_{oc} u_{\star}^3, \tag{A.1}$$

$$\Phi_{aw} = \rho_a \alpha_{aw} u_{\star}^3. \tag{A.2}$$

Here, we used $\rho_a = 1.29$ kg m$^{-3}$.

The database will be extended in the future, with a focus on parameters relevant for remote sensing applications. These include directional slope statistics for remote sensing studies, i.e., for the correction of surface salinity or altimeter sea state bias (e.g., Feng et al., 2006), and third moments of the frequency spectrum, to be used for the correction of ocean currents derived from Along-Track interferometry or Doppler analysis methods (Chapron et al., 2005). For further information and updates, the README file at the root of the database should be consulted.

**Table A.1**
Gridded parameters archived in the database

| Variable | Components | Units | Range of values | File extension |
|---|---|---|---|---|
| $H_s$ | 1 | m | 0–99 | .hs |
| $f_p$ | 1 | s$^{-1}$ | 0–1 | .fp |
| $H_{swg}$ | 1 | m | 0–99 | .hsw |
| $f_{pwg}$ | 1 | s$^{-1}$ | 0–1 | .fws |
| $\alpha_{aw}$ | 1 | Without dimensions | 0–999 | .paw |
| $\alpha_{oc}$ | 1 | Without dimensions | 0–999 | .poc |
| $U_{ss}$ | 2 | m s$^{-1}$ | 0–1 | .uss |
| $u_{\star}$ | 2 | m s$^{-1}$ | 0–5 | .ust |
| $T_S$ | 2 | m$^2$ s$^{-1}$ | 0–1 | .tus |

All parameters are described in the text except $f_{pwg}$ which is the mean period $T_{m0-1}$ of the part of the spectrum which receives energy from the wind (i.e., where $S_{in} > 0$). $f_{pwg}$ was used to define the age of the windsea in Fig. 13.

## Appendix B. Validation against altimeters

Altimeter $H_s$ measurements are presently available almost continuously over a 16-year time period from the six altimeter missions ERS-1, ERS-2, TOPEX-Poseidon, GEOSAT Follow-ON (GFO), Jason-1 and ENVISAT. Altimeters are short pulse nadir looking radars, operating at Ku-Band frequency (with additional measurements at C-Band frequency for TOPEX and Jason-1, and at S-Band for ENVISAT). The radar emitted pulses are reflected by the sea surface, at nadir, towards the satellite antenna. At zero incidence angle the reflection is mainly specular. The satellite return waveform is averaged over typically of the order of one thousand pulses, corresponding to a distance of 5 to 7 km along the ground track. From analysis and modelling of the return waveform 3 parameters are estimated: the satellite altitude over the sea surface, from which the sea surface height is deduced, the backscatter coefficient, proportional to the surface mean square slope and highly correlated with the surface wind speed, and the significant wave height. The accuracy of the $H_s$ retrieval is of the order of 0.50 m or 10%, whichever is greater, for the first generation of altimeters, onboard of ERS and TOPEX, and better for more recent instruments, onboard of ENVISAT and Jason. Although the altimeter measurements are calibrated during specific commissioning phase, just after launch, long-term monitoring of the performances is essential, revealing significant differences between $H_s$ measurements provided by the space agencies. The altimeter $H_s$ data used in this study are issued from the IFREMER CERSAT altimeter $H_s$ data base. The data base is constructed using the Geophysical Data Records (GDR) for each altimeter, and correcting $H_s$ measurements according to previous studies. For the present wave model assessment study, we used data from Jason-1 Picot et al., 2003, GEOSAT Follow-On Naval Oceanographic Office, 2002, and ENVISAT (ESA, 2002). Linear corrections that were applied to the altimeter SWH GDR are given as slope and intercept coefficients in Table B.1. The Jason GDR version b correction was estimated from comparison with 7193 collocated buoy measurements. ENVISAT and GFO corrections resulted from previous investigations (Queffeulou, 2004; Queffeulou, 2006).

Data from the altimeters and from the model outputs were collocated. For each altimeter pass (half orbit about 40–50 mn long) the model output field which is the closest, in time, of the mean value of the satellite pass time, is selected. Thus the maximum value of the time difference between model and altimeter data are 1 h 30 min. The model data fields are then interpolated to the altime-

**Table B.1**
Correction parameters for altimeter data

| Altimeter | Slope | Intercept |
|---|---|---|
| Jason | 1.0250 | 0.0588 |
| GFO | 1.0625 | 0.0754 |
| ENVISAT | 1.0585 | −0.1935 |

ter measurement locations (one measurement every 5–7 km, along track).

Then, satellite and interpolated model data are averaged along the ground track over 1° latitude steps. The number of data averaged over 1° depends on the latitude and on the altimeter sampling. It is on average of the order of 19–20 for Jason, 18–19 for GFO eand 15–16 for ENVISAT. For the analysis, only cases corresponding to a data number larger than 15 are selected for Jason and GFO, and larger than 12 for ENVISAT.

## References


Acreman, D., Jeffery, C., 2007. The use of Argo for validation and tuning of mixed layer models. Ocean Modelling 19, 53–69.

Agrawal, Y.C., Terray, E.A., Donelan, M.A., Hwang, P.A., Williams, A.J., Drennan, W., Kahma, K., Kitaigorodskii, S., 1992. Enhanced dissipation of kinetic energy beneath breaking waves. Nature 359, 219–220.

Alves, J.H.G.M., Banner, M.L., Young, I.R., 2003. Revisiting the Pierson–Moskowitz asymptotic limits for fully developed wind waves. J. Phys. Oceanogr. 33, 1301–1323.

Ardhuin, F., Jenkins, A.D., 2006. On the interaction of surface waves and upper ocean turbulence. J. Phys. Oceanogr. 36 (3), 551–557.

Ardhuin, F., Herbers, T.H.C., Jessen, P.F., O'Reilly, W.C., 2003. Swell transformation across the continental shelf. part II: validation of a spectral energy balance equation. J. Phys. Oceanogr. 33, 1940–1953. Available from: <http://ams.allenpress.com/archive/1520-0485/33/9/pdf/i1520-0485-33-9-1940.pdf>.

Ardhuin, F., Martin-Lauzer, F.-R., Chapron, B., Craneguy, P., Girard-Ardhuin, F., Elfouhaily, T., 2004. Dérive à la surface de l'océan sous l'effet des vagues. Comptes Rendus Géosciences 336, 1121–1130.

Ardhuin, F., Herbers, T.H.C., Watts, K.P., van Vledder, G.P., Jensen, R., Graber, H., 2007. Swell and slanting fetch effects on wind wave growth. J. Phys. Oceanogr. 37 (4), 908–931.

Ardhuin, F., Chapron, B., Collard, F., 2008a. Strong decay of steep swells observed across oceans. Nature Geosci. (submitted).

Ardhuin, F., Collard, F., Chapron, B., Queffeulou, P., Filipot, J.-F., Hamon, M., 2008b. Spectral wave dissipation based on observations: a global validation. In: Proceedings of Chinese-German Joint Symposium on Hydraulics and Ocean Engineering. Darmstadt, Germany.

Ardhuin, F., Rascle, N., Belibassakis, K.A., 2008c. Explicit wave-averaged primitive equations using a generalized Lagrangian mean. Ocean Modelling 20, 35–60.

Banner, M.L., Babanin, A.V., Young, I.R., 2000. Breaking probability for dominant waves on the sea surface. J. Phys. Oceanogr. 30, 3145–3160. Available from: <http://ams.allenpress.com/archive/1520-0485/30/12/pdf/i1520-0485-30-12-3145.pdf>.

Barnier, B., Madec, G., Penduff, T., Molines, J.-M., Treguier, A.-M., Sommer, J.L., Beckmann, A., Biastoch, A., Böning, C., Dengg, J., Derval, C., Durand, E., Gulev, S., Remy, E., Talandier, C., Theetten, S., Maltrud, M., McClean, J., Cuevas, B.D., 2006. Impact of partial steps and momentum advection schemes in a global ocean circulation model at eddy-permitting resolution. Ocean Modelling 56, 543–567.

Battjes, J.A., Janssen, J.P.F.M., 1978. Energy loss and set-up due to breaking of random waves. In: Proceedings of the 16th International Conference on Coastal Engineering, ASCE, pp. 569–587.

Bidlot, J.-R., Holt, M.W., 2006. Verification of operational global and regional wave forecasting systems against measurements from moored buoys. Tech. Rep. 30 WMO/TDNo.1333, World Meteorological Organization, Joint Commission on Oceanography and Marine Meteorology.

Bidlot, J.-R., Holmes, D.J., Wittmann, P.A., Lalbeharry, R., Chen, H.S., 2002. Intercomparison of the performance of operational ocean wave forecasting systems with buoy data. Weather Forecast. 17, 287–309. Available from: <http://ams.allenpress.com/archive/1520-0434/17/2/pdf/i1520-0434-17-2-287.pdf>.

Bidlot, J., Abdalla, S., Janssen, P., 2005. A revised formulation for ocean wave dissipation in CY25R1. Tech. Rep. Memorandum R60.9/JB/0516, Research Department, ECMWF, Reading, UK.

Bidlot, J., Janssen, P., Abdalla, S., 2007a. A revised formulation of ocean wave dissipation and its model impact. Tech. Rep. Memorandum 509, ECMWF, Reading, UK.

Bidlot, J.-R., Li, J.-G., Wittmann, P., Fauchon, M., Chen, H., Lefèvre, J., Bruns, T., Greenslade, D., Ardhuin, F., Kohno, N., Park, S., Gomez, M., 2007b. Intercomparison of operational wave forecasting systems. In: Proceedings of the 10th Int. Workshop of Wave Hindcasting and Forecasting, Hawaii. Available from: <http://www.waveworkshop.org/10thWaves/Papers/paper_10th_workshop_Bidlot_at_al.pdf>.

Bister, M., Emanuel, K.A., 1998. Dissipative heating and hurricane intensity. Meteorol. Atmos. Phys. 65, 233–240.

Bonekamp, H., Komen, G.J., Sterl, A., 2002. Statistical comparisons of observed and ECMWF modeled open ocean surface drag. J. Phys. Oceanogr. 32, 1010–1027.

Burchard, H., 2001. Simulating the wave-enhanced layer under breaking surface waves with two-equation turbulence models. J. Phys. Oceanogr. 31, 3133–3145.

Businger, J.A., Wyngaard, J.C., Izumi, I., Bradley, E.F., 1971. Flux-profile relationships in the atmospheric surface layer. J. Atmos. Sci. 28, 181–189. Available from: <http://ams.allenpress.com/archive/1520-0469/28/2/pdf/i1520-0469-28-2-181.pdf>.

Chapron, B., Collard, F., Ardhuin, F., 2005. Direct measurements of ocean surface velocity from space: interpretation and validation. J. Geophys. Res. 110 (C07008). doi:10.1029/2004JC002809.

Collard, F., Ardhuin, F., Chapron, B., 2005. Extraction of coastal ocean wave fields from SAR images. IEEE J. Oceanic Eng. 30 (3), 526–533.

Collard, F., Mouche, A.A., Chapron, B., Danilo, C., Johannessen, J., 2008. Routine high resolution observation of selected major surface currents from space. In: Proceedings of SEASAR 2008, SP-656. ESA, ESA - ESRIN, Frascati, Italy. Available from: <http://earth.esa.int/workshops/seasar2008/participants/287/pres_287_Collard.pdf>.

Craig, P.D., Banner, M.L., 1994. Modeling wave-enhanced turbulence in the ocean surface layer. J. Phys. Oceanogr. 24, 2546–2559. Available from: <http://ams.allenpress.com/archive/1520-0485/24/12/pdf/i1520-0485-24-12-2546.pdf>.

Craik, A.D.D., Leibovich, S., 1977. The generation of Langmuir circulations by an instability mechanism. J. Fluid Mech. 81, 209–223.

Dalrymple, R.A., 1974. A finite amplitude wave on a linear shear current. J. Geophys. Res. 79, 4498–4504.

Darbyshire, J., 1958. The generation of waves by wind. Philos. Trans. Roy. Soc. London A 215 (1122), 299–428.

Dean, R.G., 1965. Stream function representation of nonlinear ocean waves. J. Geophys. Res. 70, 4561–4572.

Dobson, F.W., 1971. Measurements of atmospheric pressure on wind-generated sea waves. J. Fluid Mech. 48, 91–127.

Donelan, M., 1990. The sea. Ocean Engineering Science, vol. 9. Wiley, New York. pp. 239–292.

Donelan, M.A., 1998. Air–water exchange processes. In: Imberger, J. (Ed.), Physical Processes in Lakes and Oceans. American Geophysical Union, Washington, DC, pp. 18–36, ISBN: 0-87590-268-5.

Donelan, M.A., 1999. Wind-induced growth and attenuation of laboratory waves. In: Sajjadi, S.G., Thomas, N.H., Hunt, J.C.R. (Eds.), Wind-Over-Wave Couplings. Clarendon Press, Oxford, UK, pp. 183–194.

Donelan, M.A., Pierson Jr., W.J., 1987. Radar scattering and equilibrium ranges in wind-generated waves with application to scatterometry. J. Geophys. Res. 92 (C5), 4971–5029.

Drennan, W.M., Taylor, P.K., Yelland, M.J., 2005. Parameterizing the sea surface roughness. J. Phys. Oceanogr. 35, 835–848.

Elfouhaily, T., Chapron, B., Katsaros, K., Vandemark, D., 1997. A unified directional spectrum for long and short wind-driven waves. J. Geophys. Res. 102 (C7), 15781–15796.

ESA, March 2002. ENVISAT RA-2/MWR Product Handbook. Tech. Rep. PO-TN-ESR-RA-0050.

Fairall, C.W., Bradley, E.F., Hare, J.E., Grachev, A.A., Edson, J.B., 2003. Bulk parameterization of air–sea fluxes: updates and verification for the COARE algorithm. J. Climate 16, 571–591.

Feng, H., Vandemark, D., Quilfen, Y., Chapron, B., Beckley, B., 2006. Assessment of wind-forcing impact on a global wind-wave model using the TOPEX altimeter. Ocean Eng. 33, 1431–1461. doi:10.1016/j.oceaneng.2005.10.015.

Garrett, C., 1976. Generation of Langmuir circulations by surface waves – a feedback mechanism. J. Mar. Res. 34, 117–130.

Gaspar, J.P., Grégoris, Y., Lefevre, J.M., 1990. A simple eddy kinetic energy model for simulations of oceanic vertical mixing: Tests at station Papa and long-term upper ocean study site. J. Geophys. Res. 95 (C9), 16179–16193.

Gemmrich, J.R., Farmer, D.M., 2004. Near-surface turbulence in the presence of breaking waves. J. Phys. Oceanogr. 34, 1067–1086.

Gemmrich, J.R., Mudge, T.D., Polonichko, V.D., 1994. On the energy input from wind to surface waves. J. Phys. Oceanogr. 24, 2413–2417. Available from: <http://ams.allenpress.com/archive/1520-0485/24/11/pdf/i1520-0485-24-11-2413.pdf>.

Grachev, A.A., Fairall, C.W., Hare, J.E., Edson, J.B., Miller, S.D., 2003. Wind stress vector over ocean waves. J. Phys. Oceanogr. 33, 2408–2429. Available from: <http://ams.allenpress.com/archive/1520-0485/33/11/pdf/i1520-0485-33-11-2408.pdf>.

Hanson, J.L., Phillips, O.M., 2001. Automated analysis of ocean surface directional wave spectra. J. Atmos. Ocean Technol. 18, 277–293.

Harcourt, R.R., D'Asaro, E.A., 2008. Large eddy simulation of Langmuir turbulence in pure wind seas. J. Phys. Oceanogr. 38, 1542–1562.

Hasselmann, K., 1970. Wave-driven inertial oscillations. Geophys. Fluid Dyn. 1, 463–502.

Janssen, P.A.E.M., 2008. Progress in ocean wave forecasting. J. Comput. Phys. 227, 3572–3594.

Janssen, P.A.E.M., Saetra, O., Wettre, C., Hersbach, H., 2004. Impact of the sea state on the atmosphere and ocean. Ann. Hydrograph. sér. 3 (772), 3-1–3-23.

Janssen, P., Bidlot, J.-R., Abdalla, S., Hersbach, H., 2005. Progress in ocean wave forecasting at ECMWF. Tech. Rep. Memorandum 478, Research Department, ECMWF, Reading, UK.

Jarosz, E., Mitchell, D.A., Wang, D.W., Teague, W.J., 2007. Bottom-up determination of air–sea momentum exchange under a major tropical cyclone. Science 315, 1707–1709.

Kantha, L.H., Clayson, C.A., 2004. On the effect of surface gravity waves on mixing in the oceanic mixed layer. Ocean Modelling 6, 101–124.

Kedar, S., Longuet-Higgins, M., Graham, F.W.N., Clayton, R., Jones, C., 2008. The origin of deep ocean microseisms in the north Atlantic ocean. Proc. Roy. Soc. London A, 1–35.

Kenyon, K.E., 1969. Stokes drift for random gravity waves. J. Geophys. Res. 74, 6991–6994.

Kerbaol, V., Chapron, B., Vachon, P., 1998. Analysis of ERS-1/2 synthetic aperture radar wave mode imagettes. J. Geophys. Res. 103 (C4), 7833–7846.

Kitaigorodskii, S.A., 1994. A note on the influence of breaking wind waves on the aerodynamic roughness of the sea surface as seen from below. Tellus A 46, 681–685.

Komen, G.J., Hasselmann, K., Hasselmann, S., 1984. On the existence of a fully developed windsea spectrum. J. Phys. Oceanogr. 14, 1271–1285.

Kudryavtsev, V.N., Makin, V.K., 2004. Impact of swell on the marine atmospheric boundary layer. J. Phys. Oceanogr. 34, 934–949.

Kudryavtsev, V.N., Makin, V.K., Chapron, B., 1999. Coupled sea surface-atmosphere model. 2. Spectrum of short wind waves. J. Geophys. Res. 104, 7625–7639.

Lamb, H., 1932. Hydrodynamics, 6th ed. Cambridge University Press, Cambridge, UK.

Langmuir, I., 1938. Surface motion of water induced by wind. Science 87, 119–123.

Li, M., Zahariev, K., Garrett, C., 1995. Role of Langmuir circulation in the deepening of the ocean surface mixed layer. Science 25, 1955–1957.

Liu, L.L., Wang, W., Huang, R.X., 2008. The mechanical energy input to the ocean induced by tropical cyclones. J. Phys. Oceanogr. 38, 1253–1266.

Long, C.E., Resio, D.T., 2007. Wind wave spectral observations in Currituck Sound, North Carolina. J. Geophys. Res. 112, C05001.

Magne, R., Belibassakis, K., Herbers, T.H.C., Ardhuin, F., O'Reilly, W.C., Rey, V., 2007. Evolution of surface gravity waves over a submarine canyon. J. Geophys. Res. 112, C01002.

McIntyre, M.E., 1981. On the'wave momentum' myth. J. Fluid Mech. 106, 331–347.

McWilliams, J.C., Restrepo, J.M., 1999. The wave-driven ocean circulation. J. Phys. Oceanogr. 29, 2523–2540.

Mellor, G., Blumberg, A., 2004. Wave breaking and ocean surface layer thermal response. J. Phys. Oceanogr. 34, 693–698.

Mellor, G.L., Yamada, T., 1982. Development of a turbulence closure model for geophysical fluid problems. Rev. Geophys. Space Phys. 20 (C2), 851–875.

Melville, W.K., Verron, F., White, C.J., 2002. The velocity field under breaking waves: coherent structures and turbulence. J. Fluid Mech. 454, 203–233.

Miche, A., 1944. Mouvements ondulatoires de la mer en profondeur croissante ou décroissante. forme limite de la houle lors de son déferlement. application aux digues maritimes. Troisième partie. Forme et propriétés des houles limites lors du déferlement. Croissance des vitesses vers la rive. Ann. Ponts Chaussées Tome 114, 369–406.

Naval Oceanographic Office, NOAA Laboratory for Satellite Altimetry, March 2002. GEOSAT Follow-On GDR User's Handbook. Tech. Rep. NOAA/NESDIS/ORA:E/RA31, 1315 East-West Highway 3620, Silver Spring, MD, USA.

Noh, Y., 1996. Dynamics of diurnal thermocline formation in the oceanic mixed layer. J. Geophys. Res. 26, 2189–2195.

Noh, Y., Kim, H.J., 1999. Simulations of temperature and turbulence structure of the oceanic boundary layer with the improved near-surface process. J. Geophys. Res. 104 (C7), 15621–15634.

Noh, Y., Min, H.S., Raasch, S., 2004. Large eddy simulation of the ocean mixed layer: the effects of wave breaking and Langmuir circulation. J. Phys. Oceanogr. 34, 720–733.

Phillips, O.M., 1958. The equilibrium range in the spectrum of wind-generated waves. J. Fluid Mech. 4, 426–433.

Phillips, O.M., 1977. The Dynamics of the Upper Ocean. Cambridge University Press, London. 336 pp.

Picot, N., Case, K., Desai, S., Vincent, P., 2003. PODAAC User Handbook. IGDR and GDR Jason products. Tech. Rep. SMM-MU-M5-OP-13184-CN (AVISO), JPL D-21352 (PODAAC).

Pierson Jr., W.J., Moskowitz, L., 1964. A proposed spectral form for fully developed wind seas based on the similarity theory of S.A. Kitaigorodskii. J. Geophys. Res. 69 (24), 5181–5190.

Polton, J.A., Lewis, D.M., Belcher, S.E., 2005. The role of wave-induced Coriolis–Stokes forcing on the wind-driven mixed layer. J. Phys. Oceanogr. 35, 444–457.

Powell, M.D., Houston, S.H., 1998. Surface wind fields of 1995 hurricanes Erin, Opal, Luis, Marilyn, and Roxanne at landfall. Mon. Weather Rev. 126, 1259–1273. Available from: <http://ams.allenpress.com/archive/1520-0493/126/5/pdf/i1520-0493-126-5-1259.pdf>.

Powell, M.D., Vickery, P.J., Reinhold, T.A., 2003. Reduced drag coefficient for high wind speeds in tropical cyclones. Nature 422, 279–283.

Queffeulou, P., 2004. Long term validation of wave height measurements from altimeters. Mar. Geod. 27, 495–510. doi:10.1080/01490410490883478.

Queffeulou, P., 2006. Altimeter wave height validation – an update. In: Proceedings of OSTST meeting, Venice, Italy, March 16–18. Available from: <http://www.jason.oceanobs.com/html/swt/posters2006_uk.html>.

Quéré, C.L., Rödenbeck, C., Buitenhuis, E.T., Conway, T.J., Langenfelds, R., Gomez, A., Labuschagne, C., Ramonet, M., Nakazawa, T., Metzl, N., Gillett, N., Heimann, M., 2007. Saturation of the Southern Ocean $CO_2$ sink due to recent climate change. Science 316, 1735–1738.

Rascle, N., 2007. Impact of waves on the ocean circulation (impact des vagues sur la circulation océanique). Ph.D. Thesis, Université de Bretagne Occidentale. Available from: <http://tel.archives-ouvertes.fr/tel-00182250/fr/>.

Rascle, N., Ardhuin, F., Terray, E.A., 2006. Drift and mixing under the ocean surface. A coherent one-dimensional description with application to unstratified conditions. J. Geophys. Res. 111, C03016. doi:10.1029/2005JC003004.

Sloss, P.W., 1993. Global relief cd-rom. Tech. rep., Marine Geology and Geophysics Division, U.S. National Geophysical Data Center (NOAA/NESDIS/NGDC/MGGD). Available from: <http://ww.ngdc.noaa.gov/mgg/global/relief/ETOPO5/readme.txt>.

Smith, J., 1998. Evolution of Langmuir circulation during a storm. J. Geophys. Res. 103 (C6), 12649–12668. Available from: <http://jerry.ucsd.edu/JSmith_PDF/1998-jgro103-Smith-LCinStorm.pdf>.

Smith, J.A., 2001. Observations and theories of Langmuir circulation: a story of mixing. In: Lumley, J. (Ed.), Fluid Mechanics and the Environment: Dynamical Approaches. Springer, New York, pp. 295–314. Available from: <http://jerry.ucsd.edu/JSmith_PDF/2001-Smith-aStoryOfMixing.pdf>.

Smith, J.A., 2006. Wave-current interactions in finite-depth. J. Phys. Oceanogr. 36, 1403–1419.

Snyder, R.L., Dobson, F.W., Elliot, J.A., Long, R.B., 1981. Array measurement of atmospheric pressure fluctuations above surface gravity waves. J. Fluid Mech. 102, 1–59.

Soloviev, A., Lukas, R., 2003. Observation of wave-enhanced turbulence in the near-surface layer of the ocean during TOGA COARE. Deep Sea Res. I 50, 371–395.

Sriver, R.L., Huber, M., 2007. Observational evidence for an ocean heat pump induced by tropical cyclones. Nature 547, 577–580.

Stacey, M.W., 1999. Simulation of the wind-forced near-surface circulation in Knight Inlet: a parameterization of the roughness length. J. Phys. Oceanogr. 29, 1363–1367.

Stacey, M.W., Pond, S., 1997. On the Mellor–Yamada turbulence closure scheme: the surface boundary condition for $q^2$. J. Phys. Oceanogr. 27, 2081–2086.

Sullivan, P.P., McWilliams, J.C., Melville, W.K., 2007. Surface gravity wave effects in the oceanic boundary layer: large-eddy simulation with vortex force and stochastic breakers. J. Fluid Mech. 593, 405–452.

Sullivan, P.P., Edson, J.B., Hristov, T., McWilliams, J.C., 2008. Large-eddy simulations and observations of atmospheric marine boundary layers above nonequilibrium surface waves. J. Atmos. Sci. 65 (3), 1225–1244.

Terray, E.A., Donelan, M.A., Agrawal, Y.C., Drennan, W.M., Kahma, K.K., Williams, A.J., Hwang, P.A., Kitaigorodskii, S.A., 1996. Estimates of kinetic energy dissipation under breaking waves. J. Phys. Oceanogr. 26, 792–807.

Terray, E.A., Drennan, W.M., Donelan, M.A., 2000. The vertical structure of shear and dissipation in the ocean surface layer. In: Proc. Symp. on Air-Sea Interaction. University of New South Wales, Sydney, pp. 239–245.

Tolman, H.L., 2002. Validation of WAVEWATCH-III version 1.15. Tech. Rep. 213, NOAA/NWS/NCEP/MMAB.

Tolman, H.L., 2003. Treatment of unresolved islands and ice in wind wave models. Ocean Modelling 5, 219–231.

Tolman, H.L., 2007. The 2007 release of WAVEWATCH III. In: Proceedings of the 10th International Workshop of Wave Hindcasting and Forecasting, Hawaii. Available from: <http://www.waveworkshop.org/10thWaves/Papers/oahu07_Q4.pdf>.

Tolman, H.L., Chalikov, D., 1996. Source terms in a third-generation wind wave model. J. Phys. Oceanogr. 26, 2497–2518.

Wang, W., Huang, R.X., 2004. Wind energy input to the surface waves. J. Phys. Oceanogr. 34, 1276–1280. Available from: <http://ams.allenpress.com/archive/1520-0485/34/5/pdf/i1520-0485-34-5-1276>.

Wang, D.W., Mitchell, D.A., Teague, W.J., Jarosz, E., Hulbert, M.S., 2005. Extreme waves under hurricane Ivan. Science 309, 896.

Weber, J.E., Førland, E., 1990. Effect of the air on the drift velocity of water waves. J. Fluid Mech. 218, 619–640.

Wessel, P., Smith, W.H.F., 1996. A global self-consistent hierarchical, high-resolution shoreline database. J. Geophys. Res. 101, 8741–8743.

WISE Group, 2007. Wave modelling-the state of the art. Prog. Oceanogr. 75, 603–674.

Wunsch, C., Ferrari, R., 2003. Vertical mixing, energy, and the general circulation of the oceans. Annu. Rev. Fluid Mech. 36, 281–314.

Xu, Z., Bowen, A.J., 1994. Wave- and wind-driven flow in water of finite depth. J. Phys. Oceanogr. 24, 1850–1866.